Next Materials 10 (2026) 101390

Contents lists available at ScienceDirect

Next Materials

journal homepage: www.sciencedirect.com/journal/next-materials

Research article

Synergistic visible-light photocatalysis by ZnO/black phosphorus nanohybrids immobilized on activated kaolinite

Pierre Ngue Song [a], Stéphanie D. Lambert [a], Antoine Farcy [a], Abdelhalim Ouhaibi [b], Louise Lejeune [c], Pierre Eloy [c], Sophie Hermans [c], Maxime Delaey [d], Dirk Poelman [d], Julien G. Mahy [a,*]

[a] Department of Chemical Engineering – Nanomaterials, Catalysis & Electrochemistry, University of Liège, B6a, Quartier Agora, Allée du six Août 11, Liège 4000, Belgium
[b] Division Milieux Ionisés et Lasers, Centre de Développement des Technologies Avancées, (CDTA), Cité du 20 aout 1956, Baba Hassen, BP n°. 17, Alger, Algeria
[c] Institute of Condensed Matter and Nanosciences - Molecular Chemistry, Materials and Catalysis (IMCN/MOST), Université catholique de Louvain, Place Louis Pasteur 1, Box L4.01.03, Louvain-La-Neuve 1348, Belgium
[d] LumiLab, Department of Solid State Sciences, Ghent University, Krijgslaan 281-S1, Ghent B-9000, Belgium

ARTICLE INFO

Keywords:
ZnO/black phosphorus nanohybrids
Activated kaolinite
Visible-light photocatalysis
Solvothermal doping
Charge separation
Polyazo dye degradation

ABSTRACT

This study reports the design and synthesis of a novel composite photocatalyst based on ZnO nanoparticles immobilized onto a black phosphorus (BP)-modified activated kaolinite matrix. The fabrication strategy combines solvothermal doping and sol-gel methods to achieve a hybrid 2D/3D semiconductor system. Comprehensive characterization, including XRD, XPS, UV-Vis DRS, PL, SEM, and TEM, confirmed the successful integration of ZnO and BP within the clay structure. The resulting composites exhibited enhanced photocatalytic activity under visible light compared to pure ZnO, as evaluated by the degradation of two polyazo dyes (Direct Red 80 and Chicago Sky Blue 6B). The Activated Clay/BP/ZnO composite showed superior performance, with first-order kinetic constants up to three times higher than those of pure ZnO. This improvement is attributed to improved charge separation, defect engineering, and strong interfacial interactions within the heterostructure. These findings highlight the potential of BP-doped clay-supported ZnO composites as efficient, sustainable photocatalysts for wastewater treatment.

1. Introduction

The application of dyeing processes enables the coloration of textiles using synthetic dyes. This represents a critical step in the textile ennoblement process, as it requires substantial water consumption [1,2]. However, it must be emphasized that this process also generates significant volumes of wastewater laden with high concentrations of dyes [3]. Most synthetic dyes are designed to be resistant to environmental conditions, such as light, temperature, microbial attack, and oxidizing agents [4]. Nevertheless, in low- and middle-income countries, it is observed that up to 80 % of dye-laden wastewater is discharged into water bodies without treatment [5]. Furthermore, the presence of dyes in aquatic ecosystems, even at low concentrations, is highly visible. It reduces sunlight penetration, while increasing biochemical oxygen demand (BOD) and chemical oxygen demand (COD) [6,7]. It is well established that the discharge of dye-rich wastewater into surrounding waters can contribute to eutrophication [8].

Under the action of microorganisms, dyes release nitrates and phosphates into the natural environment. These mineral ions serve as nutrients for microorganisms, and when introduced in large quantities, they trigger uncontrolled algal blooms in rivers and stagnant waters, leading to oxygen depletion due to the inhibition of photosynthesis at depth [9]. Additionally, the substantial oxygen consumption by aerobic bacteria, resulting from high organic matter loads, causes hypoxic conditions in aquatic environments, leading to the asphyxiation of fauna [10]. Moreover, the successive enrichment of non-degradable toxic pollutants through bioaccumulation along the food chain results in significantly elevated, and potentially hazardous, pollutant concentrations in the final consumer [11]. Additionally, dyes can decompose into more toxic xenobiotics under microbial action. For instance, carcinogenic amines may be produced from the cleavage of azo bonds in azo dyes, or leuco derivatives may form in the case of triphenylmethanes

* Corresponding author.
E-mail address: julien.mahy@uliege.be (J.G. Mahy).

https://doi.org/10.1016/j.nxmate.2025.101390
Received 6 August 2025; Received in revised form 9 October 2025; Accepted 29 October 2025
Available online 6 November 2025

[12].

On the other hand, increasingly stringent and specific environmental regulations on industrial discharges compel industries to treat their wastewater prior to release into the environment. Among various methods, advanced oxidation processes (AOPs) offer highly promising approaches for treating effluents containing organic micropollutants, as they are not specific to a particular chemical family of compounds. These processes also have the advantage of degrading organic pollutants, whereas other treatment technologies often merely transfer pollution rather than eliminate it [13]. Heterogeneous photocatalysis, an advanced oxidation process, is employed in water and air treatment. It relies on the absorption of photons with energy equal to or greater than the bandgap (E_c-E_v) by a semiconductor, enabling the transition of electrons from the valence band (E_v) to the conduction band (E_c). This generates electron vacancies, commonly referred to as holes (h^+), in the valence band, creating an oxidation-reduction system [14,15]. If their lifetime permits, electrons can be transferred to electron acceptors, while holes can be filled by electron donors [16]. Ultimately, the combination of electron (reducing agent) and hole (oxidizing agent) reactions with adsorbed electron acceptors and donors, respectively, determines the synthesis of products necessary for the photocatalytic reaction [17].

Heterogeneous photocatalysis is currently emerging as a green process for the treatment of water and wastewater [18–20]. Its future as an effective treatment method within sustainable development policies requires researchers and industrial partners to address several challenges. For fundamental research, the primary challenge remains the development of next-generation photocatalytic materials that can enhance the performance of existing catalysts under near-UV (UVA) light [21], but more importantly, enable strong activity under visible light.

Many current photocatalytic applications employ ZnO as a semiconductor due to its unique properties, namely: non-toxicity, optical transparency, high chemical and photonic corrosion resistance [4,22]. However, the main drawback of ZnO lies in its wide band gap of 3.3 eV [23,24], which limits its absorption to only 4 % of the solar spectrum during photocatalytic applications using natural light [25]. Moreover, the agglomeration of ZnO nanoparticles can reduce the available surface area, thereby impairing adsorption properties, which are combined with high electron-hole recombination rates, further limiting its performance [26]. Another major issue is the leaching of Zn^{2+} ions during photocatalytic processes [27].

To address these limitations, significant efforts have been devoted to modifying ZnO to extend its spectral response into the visible region. One common strategy is doping with metals such as Cu, Fe, Ag, Mn, and Ce [28–31], aimed at slowing down the recombination rate of electrons and holes by creating energy levels within the band gap and/or by shifting the conduction and/or valence bands [32].

Another promising approach involves incorporating secondary materials such as SiO_2, hydroxyapatite, clay, or graphite to make composite materials [33–38]. These secondary materials help prevent agglomeration of ZnO nanoparticles and reduce Zn^{2+} leaching, while improving surface adsorption. Indeed, surface properties are key to photocatalyst efficiency [32,39], as better-adsorbed organic pollutants on the photocatalyst surface can be more readily oxidized [40]. Hence, adsorbent-supported photocatalysts often outperform monolithic photocatalysts in organic pollutant degradation [41].

Immobilizing ZnO nanoparticles on a suitable matrix thus offers multiple advantages and provides a sustainable solution to ZnO's limitations as a photocatalyst. Clay minerals are ideal for this purpose due to their various nanostructures, allowing the synthesis of porous structures with large surface areas: layered (e.g., kaolinite, smectites), fibrous (e.g., sepiolite, palygorskite), or tubular (e.g., halloysite) [4,42].

Recently, in parallel, black phosphorus (BP) nanosheets, a promising 2D semiconductor material, have attracted considerable interest, particularly for their photocatalytic activity in degrading organic pollutants [43]. BP's most attractive property is its direct band gap, which is thickness-dependent and ranges from 0.3 to 2.1 eV [44]. In addition, few-layer BP's strong in-plane electronic anisotropy offers significant advantages for electronic and optoelectronic applications, such as high carrier mobility, tunable band gap, and strong light-matter interaction [45,46].

While various doping and support strategies have been explored to improve the photocatalytic efficiency of ZnO, few studies have combined a 2D semiconductor like black phosphorus with zinc oxide on a natural, porous matrix such as activated kaolinite. This approach offers a promising and low-cost platform to improve light absorption, charge separation, and pollutant adsorption in a single, multifunctional material.

The scientific objective of this work is to develop a highly active composite photocatalyst by immobilizing both a 2D and a 3D semiconductor on a common activated clay matrix. The immobilization of ZnO on an activated clay matrix doped with black phosphorus (BP) can generate several synergistic effects that enhance photocatalytic performance. Firstly, the activated clay, due to its increased specific surface area and the creation of additional reactive sites, serves as a dispersing support that limits the aggregation of ZnO nanoparticles and promotes better exposure of active sites [47]. Additionally, anchoring ZnO onto such a support can contribute to reducing the rapid recombination of electron-hole pairs while facilitating their migration to the surface. Furthermore, the incorporation of BP, a two-dimensional material with high electron mobility and tunable bandgap, provides an efficient charge transfer channel [48]. It offers the advantage of acting as a conductive bridge, enabling spatial separation of photoinduced charge carriers, which can extend their lifetime and enhance the efficiency of redox reactions [49]. Finally, such an interaction (ZnO/BP) can induce favorable band alignment, facilitating the absorption of visible light—typically limited for ZnO alone—and thus broadening the spectral window of photocatalytic activity [50].

In this study, a new composite photocatalyst was synthesized in two steps: first, doping of an activated kaolinite (previously treated thermally and chemically as described in [4]) with BP nanoparticles via solvothermal reaction; second, immobilization of ZnO nanoparticles onto this matrix via a sol-gel process.

Base materials (activated clay, ZnO) as well as intermediate composites (activated clay-BP, ZnO-BP, activated clay-ZnO) were also synthesized and characterized for comparison with the final composite and to demonstrate the benefits of the new structure. To evaluate the photocatalytic activity of the synthesized materials under visible light, two model polyazo dyes, Direct Red 80 and Direct Blue 1, were selected. These compounds are widely used in textile industries and are representative of large, aromatic, anionic pollutants with varying molecular weights, making them ideal probes to assess both adsorption capacity and photocatalytic degradation efficiency under visible light.

The novelty of this study lies in the development of a ternary photocatalytic composite, AC/BP/ZnO, combining ZnO nanoparticles immobilized on a black phosphorus (BP)-doped activated kaolinite matrix, synthesized via a scalable solvothermal and sol-gel approach. Unlike conventional ZnO-based photocatalysts, which suffer from nanoparticle aggregation, rapid electron-hole recombination, and limited visible-light absorption, this hybrid system leverages the synergistic interplay of activated kaolinite, BP, and ZnO to achieve superior photocatalytic performance.

2. Experimental section

2.1. Materials

The kaolinite clay mineral ($Al_2Si_2O_5(OH)_4$) used as matrix material was sourced from the Kribi deposit in southern Cameroon. Hydrochloric acid (HCl, 37 %) was used for chemical activation. Red phosphorus (99.99 %, Thermo Scientific) and ethylenediamine (≥99 %, Sigma-

Aldrich) were used as precursors for doping the clay-based materials with black phosphorus (BP) nanoparticles [44]. Absolute ethanol was employed for washing BP-doped clay materials. Milli-Q water was used as the synthesis solvent and for washing some of the composites. Zinc acetate dihydrate ($Zn(CH_3COO)_2{\cdot}2H_2O$) and sodium hydroxide (NaOH) were used as precursor and precipitating agent, respectively. Finally, the polyazo textile dyes Direct Blue 1 (also called Sky Blue 6B) and Direct Red 80 (also called Sirius Red) were used as model pollutants (Sigma-Aldrich).

2.2. Activation of clay material by thermal and chemical treatment

The clay was washed, purified, thermally treated at 800 °C, and chemically activated by acid leaching in 6 M HCl at 110 °C to obtain the activated clay used throughout this study. Optimization procedures and exact treatment conditions are detailed in [4,51]. This material is referred to as AC (Activated Clay).

2.3. Synthesis of pure ZnO

Pure ZnO was synthesized via a co-precipitation method. For this, 5 g of zinc acetate dihydrate were dissolved in 55 mL of Milli-Q water and stirred vigorously at room temperature for 10 min until complete dissolution. The solution was then heated to 85 °C under stirring for 1 h. While maintaining the temperature at 85 °C, 100 mL of a 0.5 M NaOH solution was slowly added dropwise using a burette, leading to the formation of a precipitate. The suspension was kept under stirring at 85 °C for 3 h. After cooling to room temperature, the mixture was left undisturbed for 12 h. The precipitate was recovered by centrifugation, washed several times with Milli-Q water, and dried in an oven at 105 °C for 24 h.

2.4. Doping of pure ZnO and activated clay matrices with black phosphorus

Doping with BP nanoparticles was carried out via a solvothermal method using ethylenediamine as solvent and red phosphorus as precursor [44].

3 g of pure ZnO or activated clay and 0.75 g of red phosphorus were first ground using a planetary ball mill. The resulting powder was dispersed in 75 mL of ethylenediamine and stirred for 4 h at room temperature. The mixture was then transferred into a 100 mL Teflon-lined stainless steel autoclave and heated in a programmable chamber furnace (THERMCONCEPT) to 200 °C (heating rate of 5 °C/min). Once at 200 °C, the temperature was held for 24 h. The system was cooled down naturally to 40 °C before the autoclave was opened. After reaching room temperature, the product was recovered, washed four times with absolute ethanol, and vacuum-dried in an oven at 60 °C.

2.5. Immobilization of ZnO on AC or AC/BP surface

ZnO immobilization followed the same procedure as pure ZnO synthesis (see Section 2.3), with the only modification being the addition of 2 g of AC or AC/BP immediately after the zinc acetate dissolution. All subsequent steps remained identical. Two composite powders were obtained: AC/ZnO and AC/BP/ZnO.

2.6. Materials characterization

X-ray diffraction (XRD) was performed using a Bruker D8 Twin-Twin powder diffractometer with Cu-Kα radiation over a 2θ range of 2–70°, with a step size of 0.02° and a scan rate of 2°/min.

Elemental analysis (Si, Al, P, Zn, Ti) was carried out using inductively coupled plasma–optical emission spectrometry (ICP-OES) on an Agilent 5800 instrument. Prior sample digestion was performed using HF, following the method described by Mahy *et al.* [52].

Zeta potential was measured using a Beckman Coulter Delsa Nano C particle analyzer. A 10 mg sample was ultrasonically dispersed in 10 mL of Milli-Q water. The measuring cell was first rinsed with Milli-Q water, followed by the sample suspension.

Diffuse Reflectance Spectroscopy (DRS) was recorded from 200 to 800 nm using a PerkinElmer Lambda 1050 UV-Vis/NIR spectrophotometer equipped with a Spectralon-coated integrating sphere, photomultiplier (PMT), and InGaAs detectors. The spectra were transformed using the Kubelka–Munk function to allow band gap estimation and comparison between samples. $BaSO_4$ was used as the reference. Calculation details are given in [52].

XPS analyses are done by using a SSI-X-probe 100/206 spectrometer (Surface Science Instruments), equipped with a floodgun (8 eV) for surface charge neutralization. Samples on an adhesive support are introduced into a Macor® carousel topped by a nickel grid to avoid charge effects. Analyses are done at room temperature with an analysis chamber pressure of 10^{-6} Pa. Data treatment is executed with the CasaXPS software (Casa Software Ltd., Teignmouth, UK) using a Gaussian/Lorentzian (85/15) decomposition treatment and a Shirley-type baseline subtraction. All XPS spectra are calibrated using the C–(C,H) component of the C 1 s peak localized at 284.8 eV.

Photoluminescence (PL) spectra were recorded at room temperature using an Edinburgh Instruments FLS920 fluorimeter with a 450 W xenon arc lamp. Emission spectra were collected between 400–720 nm at 365 nm excitation, and excitation spectra (250–550 nm) were measured at 600 nm emission.

Scanning Electron Microscopy (SEM) was performed on a TESCAN Clara microscope at 15 kV. Samples (1–2 mg) were ultrasonically dispersed in 3 mL acetone. One drop was deposited on a glass slide, dried at 60 °C, gold-coated, and mounted on carbon tape.

High-resolution TEM and STEM-EDX imaging were conducted on a Thermo Scientific Talos F200i microscope at 200 kV. Samples were ultrasonically dispersed in ethanol, drop-cast on carbon-coated copper grids, and plasma-cleaned under Ar/O_2 (75 %/25 %) to remove surface carbon contamination.

2.7. Photocatalytic degradation of polyazo dyes

Photocatalytic activity was evaluated by degrading Direct Blue 1 (DB1) and Direct Red 80 (DR80) under visible light ($\lambda > 395$ nm) at 20 °C. For each dye, experiments were conducted in triplicate using a multi-sample photoreactor [52,53] equipped with a 300 W halogen lamp (220 V) emitting from 395 to 800 nm and fitted with a UV cut-off filter. The lamp was centered in a double-walled glass reactor with circulating thermostated water to dissipate heat. Aluminum foil shielded the setup from ambient light. The distance between the lamp and the samples is 2 cm.

Each sealed test tube received 10 mL of dye solution (20 mg/L) and 10 mg of photocatalyst. The suspension was stirred magnetically in the dark for 30 min to reach adsorption–desorption equilibrium (confirmed by 24 h adsorption studies). Samples were collected at 0, 2, 4, 6, 8, and 24 h, centrifuged, and analyzed by UV-Vis spectrophotometry (Genesis 10S, Thermo Scientific) at 620 nm (DB1) and 528 nm (DR80). Residual concentrations were interpolated from calibration curves.

Photodegradation efficiency was calculated using:

$$DC\ (\%) = (1 - C_t/C_0) \times 100 \quad (1)$$

where C_0 is the initial dye concentration and C_t the concentration at time t.

Control tests confirmed no photolysis occurred under visible light in the absence of photocatalyst.

In order to assess the stability of the AC/BP/ZnO composite material photocatalytic activity, recycling experiments are done on DR80 degradation under visible light. These tests consist of doing successive photocatalytic experiments on the samples with centrifugation and

washing steps in between, ultrasonic bath is used to resuspend the samples. After 8 h of the DR80 photocatalytic test described above, the catalysts are recovered by centrifugation (15,000 rpm for 20 min). Then, the same test is executed again for another 8 h. This recycling is made 5 successive times under visible light, corresponding to 40 h of total irradiation.

Triethanolamine (TEOA, 1 mmol), isopropanol (IPA, 1 mmol), and p-benzoquinone (PB, 1 mmol) are used as, respectively, hole, hydroxyl radical and superoxide scavenger in DR80 aqueous solution filled with AC/BP/ZnO sample to reach a 1 g/L concentration, inspired by [54]. Measurements are performed after 2 h (under visible light) using a UV/visible spectrophotometer at a wavelength of 528 nm.

3. Results and discussion

3.1. Mineralogical analysis by X-ray diffraction (XRD)

Fig. 1 show the X-ray diffraction patterns of the various samples. The pure ZnO sample exhibits the characteristic peaks of the wurtzite crystalline phase. The activated clay (AC) shows peaks corresponding to quartz and anatase, consistent with earlier observations [51].

For the BP-doped samples (ZnO/BP and AC/BP), the diffraction patterns indicate that the solvothermal doping at 200 °C in ethylenediamine does not alter their crystal structure. The XRD profiles also confirm the successful immobilization of ZnO nanoparticles on both clay supports (AC/ZnO and AC/BP/ZnO), evidenced by the presence of three

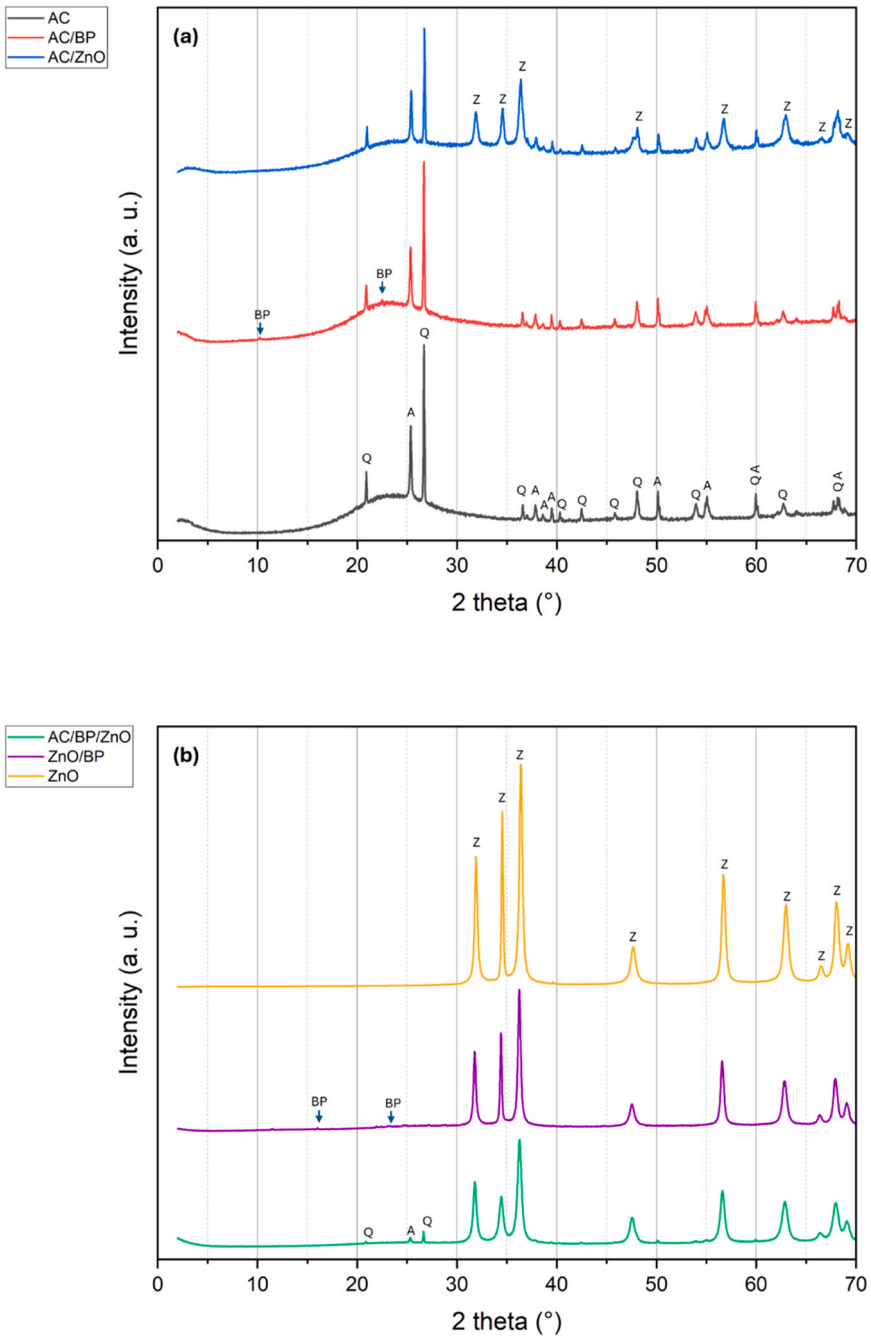

Fig. 1. X-ray diffraction (XRD) patterns of (a) AC, AC/BP, AC/ZnO and for (b) AC/BP/ZnO, ZnO/BP, ZnO samples. Reference peak positions of the different phases of the samples are indicated directly on the diffractograms by the following letters (In order not to overload the figures, phase peaks already assigned for other samples are not re-indicated): (A) anatase, (Q) quartz, (Z) wurtzite, (BP) black phosphorus.

major peaks between 2θ = 30° and 40°, characteristic of the wurtzite ZnO phase with space group P6₃mc (JCPDS 36–1451).

The diffraction peaks at 2θ = 31.8°, 34.5°, 36.3°, 47.6°, 56.6°, 62.8°, 66.5°, 68.1°, and 69.1° correspond to the (001), (002), (101), (102), (110), (103), (200), (112), and (201) wurzite planes, respectively [55, 56]. No peak associated to P species is detected.

In the XRD diffractogram of the ZnO/BP composite (Fig. 1b), two low-intensity diffraction peaks were detected at 17.3° and 27.2°, corresponding to the (020) and (021) crystallographic planes of the black phosphorus (BP) structure (JCPDS card no. 76–1957). However, it should be noted that the peak at 17.3° shifts to approximately 10° or 11° in the clay-based composites (AC/BP, Fig. 1a). Furthermore, compared to pure ZnO (Fig. 1b), a significant reduction in the intensity of the characteristic ZnO reflection peaks is observed across all composites (ZnO/BP, AC/ZnO, and AC/BP/ZnO). This reduction is most pronounced in the AC/ZnO composite (Fig. 1a), followed by AC/BP/ZnO, and least evident in ZnO/BP. The decrease in the intensity of ZnO reflection peaks in the composites (ZnO/BP, AC/ZnO, and AC/BP/ZnO) compared to pure ZnO, as well as the reduced intensity of quartz and anatase peaks following ZnO immobilization on the AC/BP matrix, can be primarily attributed to a combination of structural and dispersion effects. Similarly, the shift of one BP reflection peak in the AC/BP and AC/BP/ZnO composites follows the same trend. On one hand, the presence of an activated clay matrix (AC or AC/BP) as a support induces a dilution effect, as the relative fraction of crystalline ZnO detected is lower than in the pure ZnO sample, resulting in proportionally reduced peak intensities [57,58]. On the other hand, anchoring ZnO onto such a matrix restricts crystallite growth and promotes their dispersion as smaller nanoparticles, leading to reduced crystallinity and, consequently, broader and less intense diffraction peaks [59]. Additionally, interfacial interactions between ZnO, activated kaolinite, and BP may introduce lattice defects and disrupt long-range order, further contributing to the attenuation of diffraction signals [60]. Finally, the presence of an amorphous halo from the support or lamellar phases such as BP increases the background, which can reduce the relative contrast of ZnO peaks [61]. These phenomena collectively indicate effective dispersion and successful integration of ZnO within the composite architecture.

3.2. Chemical composition by ICP-OES

Table 1 presents the ICP-OES results for five major elements (Si, Al, Ti, P, Zn), allowing quantitative tracking of their evolution across different composites.

The relatively stable contents of silicon and aluminum in the various clay-based samples confirm the preservation of the aluminosilicate nature of the matrix. Ti is present in natural clay. Phosphorus contents of 3.98 wt% (AC/BP) and 3.85 wt% (AC/BP/ZnO) clearly confirm the successful BP doping.

Moreover, the high Zn content, averaging ~39 wt%, measured by ICP-OES in ZnO-containing samples confirms the significant presence of ZnO, in good agreement with the XRD findings and the theoretical values from the synthesis (Fig. 1).

These ICP results are further supported by the presence of the same major elements (Si, Al, Ti, P, Zn) in the XPS spectra of the same composites (see Section 3.3 and Fig. 2), offering cross-validation of the chemical composition.

Table 1
Chemical composition of samples measured by ICP-OES.

Samples	Al (wt%)	Si (wt%)	Ti (wt%)	P (wt%)	Zn (wt%)
AC	0.92	37.10	2.07	0.04	0.01
AC/BP	0.72	35.40	1.85	3.98	0.03
AC/ZnO	0.90	37.05	1.95	0.04	30.9
AC/BP/ZnO	0.70	35.37	0.70	3.85	36.4

3.3. XPS analysis of composite photocatalysts

XPS analysis was performed on the 6 samples of the study to determine their surface chemical composition and the oxidation states of key elements. The resulting spectra are shown in Fig. 2.

The XPS survey spectra of all materials confirmed the presence of major elements Zn, O, P, Si, and Al, along with trace amounts of Na, C, and N, likely originating from residual synthesis by-products or intrinsic to the clay. These elemental profiles are consistent with the ICP-OES results in Table 1, except for Ti, which was not detected by XPS due probably to its low surface concentration.

The detection of Zn, BP, and clay elements confirms the coexistence of ZnO, black phosphorus, and activated clay within the composite matrices.

Despite the physicochemical activation treatment applied to kaolinite, the aluminosilicate nature of the activated clay (AC, Fig. 2a) is confirmed by the presence of characteristic Si 2p and Al 2p binding energy peaks at 104 eV and 75 eV, respectively. However, following BP doping of AC via solvothermal treatment in ethylenediamine at elevated temperature (Fig. 2b), a shift in these binding energies to lower values, namely 102 eV for Si 2p and 73 eV for Al 2p, was observed. This shift in the characteristic Si 2p and Al 2p peaks to lower binding energies after BP doping is primarily attributed to charge transfer and a modification of the electronic environment surrounding silicon and aluminum atoms. The incorporation of BP, a semiconductor material rich in electrons, enhances the electron density around Si and Al atoms, reducing the energy required to extract an electron from their 2p orbitals, which manifests as the observed shift to lower binding energies in the XPS spectra [62]. Additionally, the potential formation of new interfacial bonds, such as Si-O-P and Al-O-P, along with disruptions to pre-existing Si-O-Al bonds, may alter the electrostatic field experienced by these atoms, further contributing to the relaxation of binding energies [63]. This is consistent with the observed decrease in the O 1 s peak binding energy from 533.5 eV in AC to 531 eV after BP doping. Moreover, the solvothermal treatment at 200°C promotes intimate anchoring of BP onto AC, which may introduce structural defects or charge redistribution within the lattice, enhancing the electron shielding effect and contributing to the observed energy shift.

High-resolution Zn 2p spectra (Fig. 2c, main survey) show two well-defined peaks at binding energies of 1021.5 eV and 1044.5 eV, corresponding to Zn $2p_{3/2}$ and Zn $2p_{1/2}$, respectively. These values confirm the presence of divalent zinc (Zn^{2+}) in the ZnO structure [64–66].

The O 1 s region provided further insights into interfacial interactions. For pure ZnO (Fig. 2c), the main O 1 s peak appears at 530.4 eV. In contrast, in AC/ZnO (Fig. 2d), ZnO/BP (Fig. 2e) and AC/BP/ZnO (Fig. 2f) composites, the O 1 s peak shifts to 531.9 eV, 531.0 eV and 531.5 eV, respectively, suggesting a modified electronic environment due to interfacial bonding with BP and the clay matrix. A similar phenomenon was reported by Yu et al. [66] for ZnO nanoparticles supported on halloysite nanotubes.

Moreover, the high-resolution spectra of the P 2p region for AC/BP (Fig. 2b) reveals a broad peak centered at 132.0 eV. This binding energy is attributed to a mixed signal from the 2p electrons of oxidized black phosphorus (BP) atoms. However, this binding energy shifts to 133.0 eV and 133.4 eV in the ZnO/BP (Fig. 2e) and AC/BP/ZnO (Fig. 2f) composites, respectively. The shift of the P 2p binding energy to higher values is primarily explained by changes in the oxidation state of phosphorus and its chemical environment, driven by chemical interactions and charge transfer with accompanying phases [67]. In the AC/BP sample, the signal at approximately 132 eV typically corresponds to partially oxidized elemental phosphorus or underdeveloped PxOy states (mixed P-P/P-Ox), indicating that BP sheets are either relatively intact or only slightly oxidized [68]. In contrast, the introduction of ZnO in the composites (ZnO/BP or AC/BP/ZnO) triggers several mechanisms that lead to a shift toward higher binding energies (133.0–133.4 eV). On one hand, ZnO, an oxidizing phase and relative electron acceptor

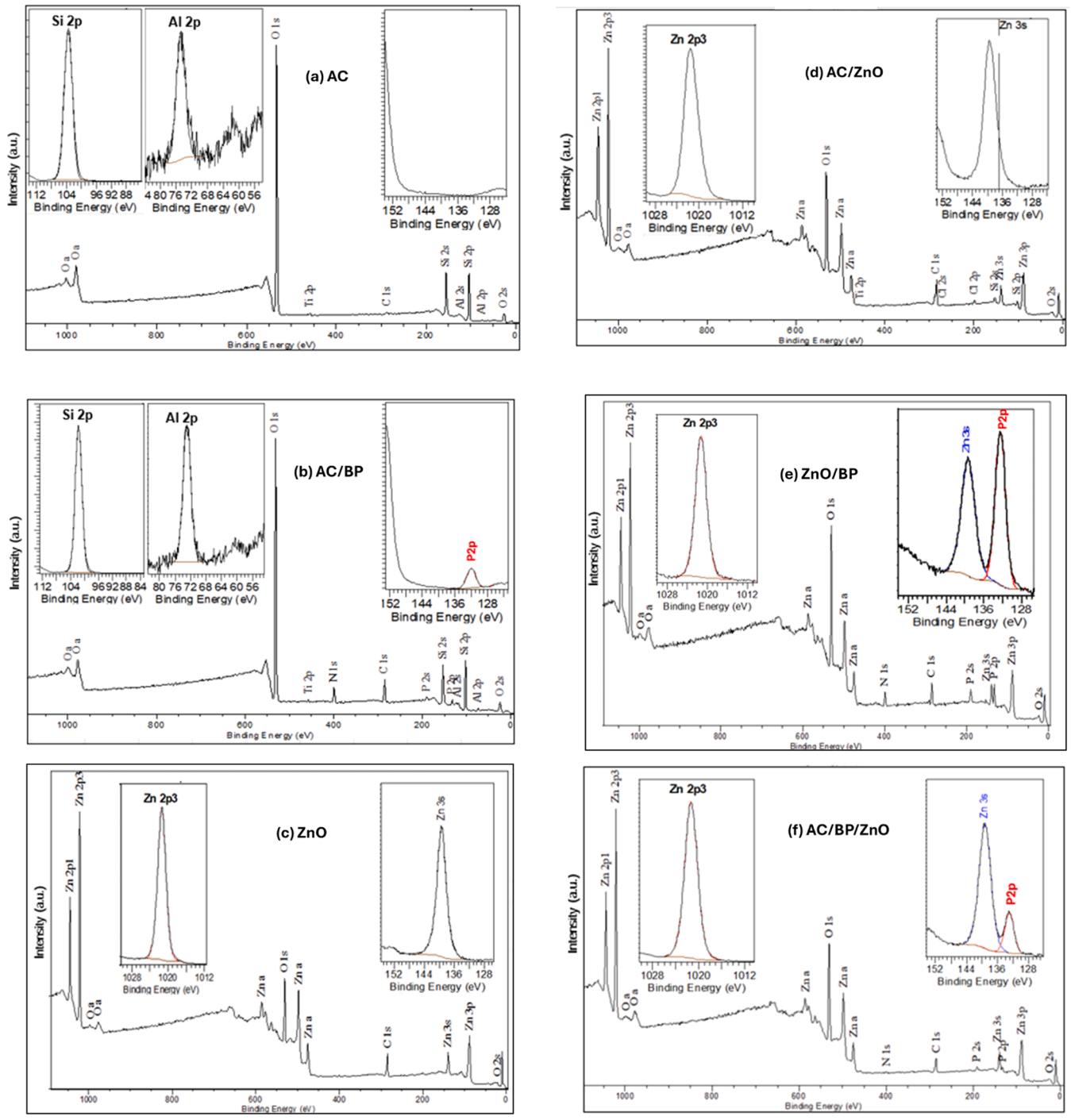

Fig. 2. XPS spectra of (a) AC, (b) AC/BP, (c) pure ZnO, (d) AC/ZnO, (e) ZnO/BP, and (f) AC/BP/ZnO. Insets highlight Si 2p, Al 2p and P 2p in (a,b), Zn 2p3/2 and 3 s in (c, d), and P 2p and Zn 3 s regions in (e,f), respectively.

compared to BP, promotes further oxidation of phosphorus or the formation of interfacial P-O-Zn/oxy-phosphate bonds during intimate contact (via sonication, hydrothermal, solvothermal, or mild calcination processes). This increases the effective oxidation state of phosphorus (trending toward partial P(+V) in oxygenated environments) [69,70]. This loss of electron density around phosphorus results in the observed XPS shift to higher binding energies.

3.4. UV–visible diffuse reflectance spectroscopy (DRS)

The UV-Vis diffuse reflectance spectra of pure ZnO and the composites ZnO/BP, AC/ZnO, and AC/BP/ZnO are shown in Fig. 3. Pure ZnO exhibits a strong absorption band centered around 345 nm, consistent with its wide band gap (~3.30 eV). This strong absorption in the near-UV region is attributed to the direct electronic transition from the valence band to the conduction band [55,71].

In contrast, the clay matrices (AC and AC/BP) do not exhibit any exploitable absorption features due to their insulating and non-semiconducting nature [66,72,73].

The ZnO/BP composite displays a red-shifted absorption tail extending into the visible range, indicating improved light harvesting capabilities. This shift could be attributed to the presence of BP

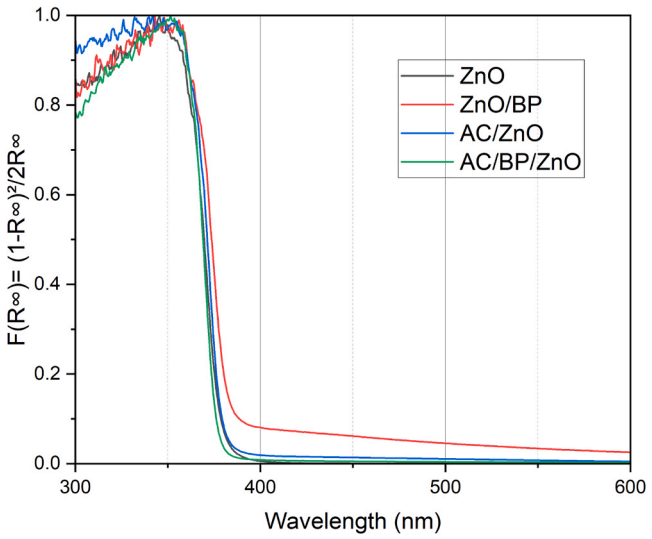

Fig. 3. UV–Vis diffuse reflectance spectra of ZnO, ZnO/BP, AC/ZnO, and AC/BP/ZnO.

intimately mixed with ZnO, which possesses a narrower band gap (<2 eV), allowing for visible-light absorption [64,66]. Or the presence of many defects in the ZnO/BP composite.

Interestingly, the absorption spectra of AC/ZnO and AC/BP/ZnO composites remain very similar to that of pure ZnO, without significant red-shift. This may result from the relatively low BP content in the ternary composite or because BP is more intimately mixed with AC than with ZnO.

The band gap energies of all photocatalysts were estimated using the Tauc plot derived from the Kubelka–Munk function. The calculated band gaps were: ZnO: 3.30 eV; ZnO/BP: 3.23 eV; AC/ZnO: 3.29 eV; AC/BP/ZnO: 3.29 eV.

These values confirm that while ZnO/BP exhibits a slight narrowing of the band gap due to BP incorporation, the two other composites retain optical properties similar to pure ZnO. However, their performance cannot be explained by band gap alone and must also consider surface/interface effects and defect states.

3.5. Photoluminescence (PL) analysis of the composites

In addition to UV–visible absorption, the photoluminescence (PL) response provides crucial information on the recombination behavior of photogenerated charge carriers. To better understand the photocatalytic performance of the materials, PL emission and excitation spectra were recorded and compared, particularly between pure ZnO and the ternary composite.

Among all tested samples, only pure ZnO and the AC/BP/ZnO composite exhibited detectable photoluminescence. Fig. 4a shows the solid-state PL emission spectra recorded at room temperature under 365 nm excitation for both materials.

These spectra offer insights into charge recombination and migration phenomena within the ZnO structure and its composite. It is well established that interface-related charge separation and recombination strongly influence fluorescence intensity in semiconductors [74]. A higher PL intensity generally correlates with faster recombination of photogenerated electrons (e^-) and holes (h^+), which results in reduced photocatalytic performance [54].

For pure ZnO (black curve in Fig. 4a), a strong orange-red emission is observed around 600 nm, typically associated with oxygen vacancy defects [75,76]. In contrast, the AC/BP/ZnO composite displays two lower-intensity peaks centered around 430 nm and 575 nm.

The first emission (430 nm, violet region) likely originates from Zn interstitial defects [75]. The second emission (575 nm, orange-red region) is attributed to oxygen vacancy-related states in the immobilized ZnO [24].

Notably, the reduced PL intensity of AC/BP/ZnO compared to pure ZnO indicates a lower recombination rate of photogenerated charge carriers, supporting the enhanced photocatalytic activity observed (observed in Section 3.8). This behavior is likely due to: (i) The BP-doped activated clay acting as an electron sink and physical support; (ii) The formation of an AC/BP/ZnO heterojunction; (iii) The presence of engineered defects in the immobilized ZnO structure.

Fig. 4b presents the excitation spectra monitored at 600 nm emission, showing how excitation wavelength influences luminescence. The AC/BP/ZnO composite reveals two distinct excitation bands, around 275 nm and 372 nm, while pure ZnO exhibits a single band at 372 nm, in line with literature data [76].

These excitation bands correspond to the PL emissions seen in Fig. 4a: (i) The 275 nm excitation leads to violet emission (400–449 nm), (ii) The 372 nm excitation induces orange-red emission (593–605 nm).

This spectral response suggests the presence of multiple defect levels in AC/BP/ZnO, enabling more efficient charge separation and surface interaction.

3.6. Zeta potential measurement

Given the observed differences in adsorption behavior among the materials (see Section 3.8), it was essential to evaluate their surface charge under near-neutral pH. Zeta potential measurements were therefore conducted to elucidate the electrostatic interactions between the photocatalysts and the anionic azo dyes.

Table 2 presents the zeta potential values of the various materials measured at pH 7.2–7.5 and 25 °C. These values reflect the surface charge of each sample and offer insight into their colloidal stability and possible electrostatic interactions with pollutants.

Pure ZnO, synthesized via co-precipitation, exhibits a positive zeta potential of + 22.36 mV, consistent with previously reported values under similar pH conditions [24,77]. However, following solvothermal treatment in ethylenediamine with red phosphorus (to produce ZnO/BP), the surface charge reverses sharply to −12.29 mV. This inversion is a direct consequence of BP nanoparticle incorporation, which seems to introduce negatively charged species at the surface.

Activated clay (AC) exhibits a strongly negative zeta potential of −21.50 mV, a typical value for kaolinite-based materials [78,79]. After BP doping, the zeta potential of AC/BP changes only slightly to −20.21 mV, indicating that the overall surface chemistry remains predominantly anionic.

Interestingly, ZnO immobilization on the clay matrix significantly alters the surface charge. The zeta potential of AC/ZnO increases to −10.55 mV, suggesting a partial neutralization of the surface by ZnO nanoparticles or a compensation of the charges. For the ternary composite AC/BP/ZnO, the surface becomes positively charged again (+9.64 mV), indicating strong ZnO–BP–clay interactions and possibly improved colloidal stability under neutral conditions.

These results emphasize the role of BP and the clay matrix in modulating surface charge, which can significantly influence adsorption behavior and photocatalytic efficiency through electrostatic interactions with charged organic pollutants.

3.7. Morphological analysis of the samples

3.7.1. SEM micrographs of composite materials

Fig. 5 presents the SEM micrographs of ZnO/BP, AC, and AC/BP/ZnO samples. These three are representative of their respective material categories, as no major morphological differences were observed between ZnO and ZnO/BP, AC and AC/BP, or AC/ZnO and AC/BP/ZnO under SEM imaging.

In Fig. 5a, the ZnO/BP composite reveals ZnO nanoparticles with

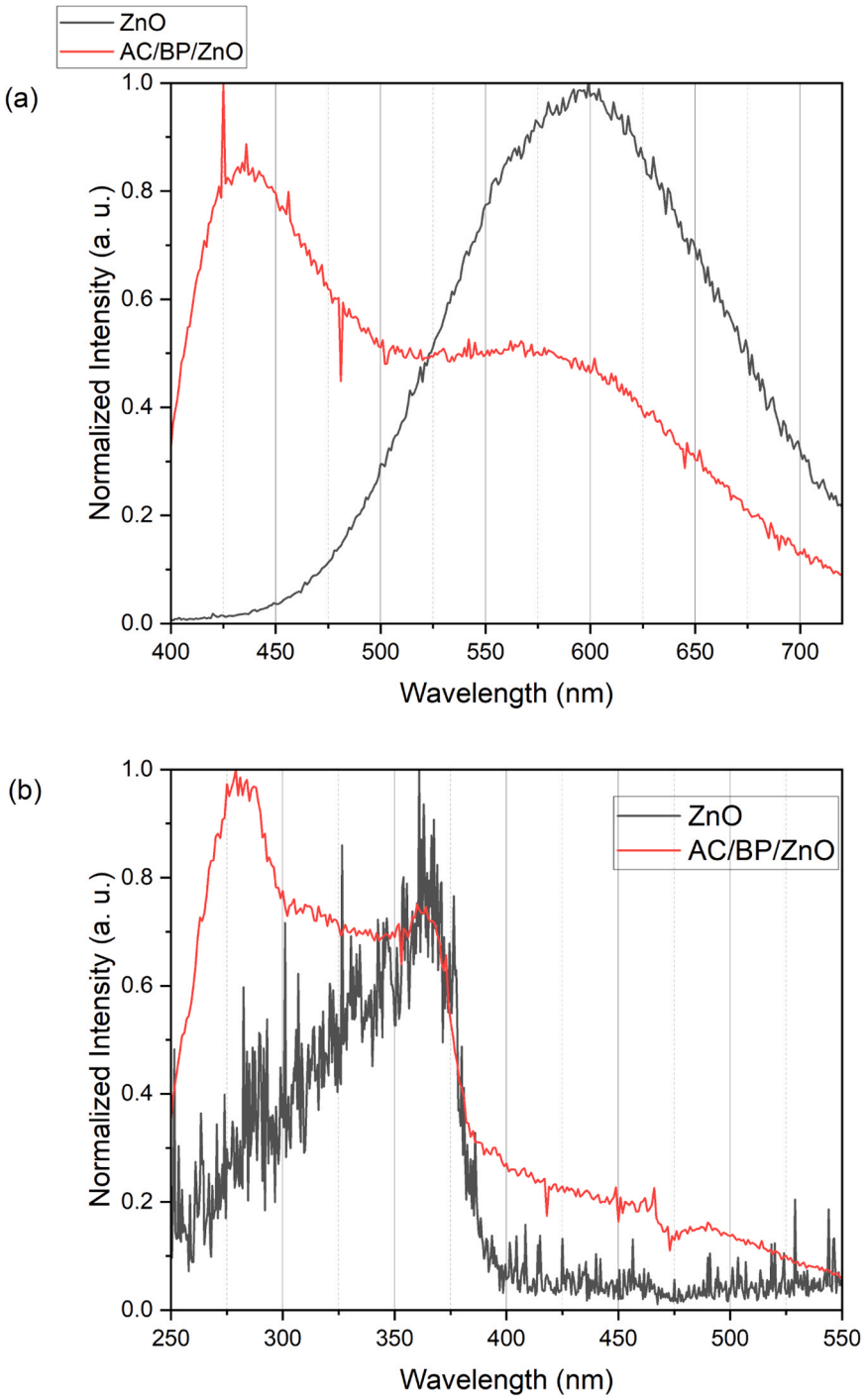

Fig. 4. (a) Normalized PL emission spectra (400–720 nm) under 365 nm excitation and (b) Normalized Excitation spectra (250–550 nm) recorded at 600 nm emission.

Table 2
Zeta potential (mV) of the synthesized materials at pH 7.2–7.5 and 25 °C.

Samples	Zeta potential (mV)
ZnO	+ 22.36
ZnO/BP	−12.29
AC	−21.50
AC/BP	−20.21
AC/ZnO	−10.55
AC/BP/ZnO	+ 9.64

spherical nanostructures, though highly agglomerated into larger aggregates. Such aggregation behavior has also been observed by Farcy *et al.* [24] in their various ZnO nanomaterial synthesis pathways. Pure ZnO has the exact same aspect.

Fig. 5b displays the layered, sheet-like morphology of the clay matrix, preserving the typical two-dimensional structure of the original kaolinite [4,51]. Upon ZnO immobilization (Fig. 5c), spherical ZnO particles are heterogeneously distributed across the surface and within the porous structure of the clay, forming irregular aggregates anchored to the matrix but less aggregated that without the clay.

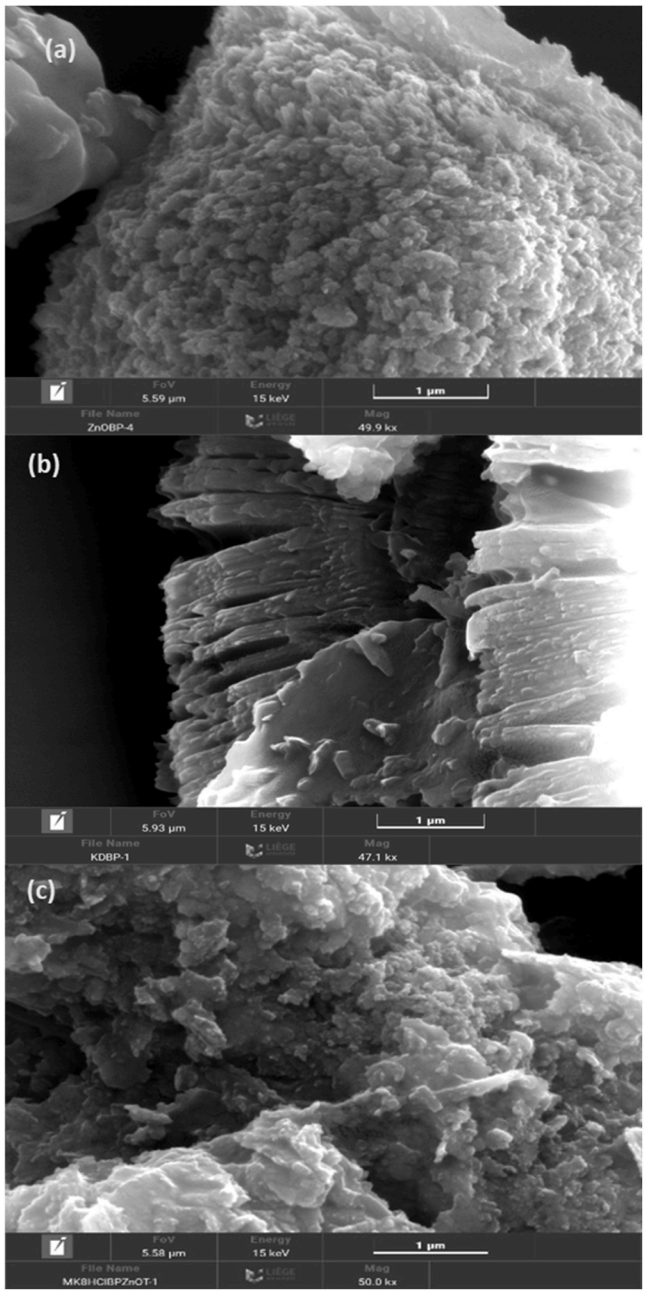

Fig. 5. SEM micrographs of (a) ZnO/BP, (b) activated clay (AC), and (c) AC/BP/ZnO.

3.7.2. *STEM-EDX and HRTEM analysis of AC/BP/ZnO composite*

High-resolution morphological and compositional mapping of the AC/BP/ZnO composite is shown in Fig. 6. STEM images (Fig. 6a and b) clearly reveal spheroidal ZnO/BP clusters formed by nanocrystals immobilized on the surface of the clay matrix.

Local EDX analysis confirms the presence of Zn, O, P, Al, and Si at the surface (Fig. 6e to j), verifying the successful deposition and surface coverage of both ZnO and BP nanoparticles on the activated clay.

The heterostructure AC–BP–ZnO was further confirmed by HRTEM imaging (Fig. 6c and d). The images show polycrystalline domains corresponding to clay, ZnO, and BP, with an average particle size of ~20 nm. Lattice fringe analysis reveals an interplanar spacing of 0.26 nm for the adjacent (002) planes of ZnO, matching the hexagonal phase (JCPDS 36–1451). The corresponding spacing for BP nanocrystals is 0.21 nm, consistent with prior reports [80,81].

These observations confirm the formation of a ternary heterostructured composite in which ZnO and BP nanoparticles are well-dispersed and tightly interfaced with the porous clay framework.

3.8. *Photocatalytic activity*

To assess the potential of the AC/BP/ZnO composite, photocatalytic degradation experiments were conducted using two model polyazo dyes, Direct Blue 1 (DB1) and Direct Red 80 (DR80), under visible light irradiation.

Fig. 7a and b show the photocatalytic degradation profiles of DR80 and DB1, respectively, for all synthesized materials.

Control experiments confirmed that no photolysis occurred for either dye under visible light alone.

For pure ZnO and ZnO/BP, two catalyst concentrations were tested: 1 g/L and 0.4 g/L. This was to fairly compare with the composites, which were tested at 1 g/L total mass, but contain only ~40 wt% ZnO (Table 1) i.e., an effective ZnO concentration of 0.4 g/L.

The activated clays (AC and AC/BP) exhibited no photocatalytic activity and only about 3 % adsorption of each dye after 24 h (adsorption measurement performed for 24 h in the dark).

Before irradiation, adsorption equilibrium was evaluated for each sample. It was found to be reached after 30 min and remained unchanged over 24 h. This equilibrium point is indicated in Figs. 7a and 7b as the C/C_0 values after 30 min of dark stirring.

The materials showed varying degrees of adsorption:

For DR80, pure ZnO at 1 g/L adsorbed approximately 36 % of the dye, while this dropped to 15 % at 0.4 g/L. The AC/BP/ZnO composite adsorbed around 28 %, AC/ZnO 24 %, and ZnO/BP about 20 % at 1 g/L, falling to 8 % at 0.4 g/L.

For DB1, adsorption was generally stronger: pure ZnO at 1 g/L adsorbed ~40 %, decreasing to 15 % at 0.4 g/L. ZnO/BP adsorbed ~34 % at 1 g/L and ~13 % at 0.4 g/L. The AC/ZnO and AC/BP/ZnO composites adsorbed ~36 % and ~40 %, respectively.

These results show that DB1 is better adsorbed than DR80, likely due to its lower molecular weight (992.8 g/mol) and smaller molecular size, which allow better diffusion into the porous clay matrix and also less steric hindrance at the catalyst surface. In contrast, DR80 (1373.07 g/mol) is bulkier and so more difficult to access the porosity. Adsorption efficiency is thus influenced by both zeta potential (Table 2) and molecular size, as also shown in previous studies [82,83].

The photodegradation kinetics (pseudo-first order) are summarized in Table 3. Pure ZnO outperformed ZnO/BP for both dyes and both concentrations, probably due to the highest recombination rate in ZnO/BP. As expected, increasing the photocatalyst concentration from 0.4 g/L to 1 g/L enhanced degradation performance.

The AC/ZnO composite, despite containing only 0.4 g/L ZnO, performed comparably to ZnO/BP at 1 g/L, demonstrating the benefit of dispersing ZnO nanoparticles on a porous clay support (as observed on Fig. 5).

The AC/BP/ZnO composite exhibited the highest photocatalytic efficiency of all samples. This synergistic performance aligns with the reduced PL emission observed in Fig. 4a, indicating improved charge separation.

The enhanced activity is likely due to: (i) The formation of a heterostructure with ZnO nanocrystals containing oxygen and zinc vacancies (Fig. 4), (ii) Efficient immobilization and dispersion of ZnO on a BP-doped activated clay support, (iii) A spongy texture of the clay (Fig. 5), which improves surface contact and accessibility. These findings are consistent with those reported by Ye *et al.* [54] for heterojunction ZnO/CeO_2 supported on tubular halloysite.

Based on kinetic constants, the degradation of DR80 and DB1 with AC/BP/ZnO is 2–3 times faster than with pure ZnO.

To assess the reusability and long-term stability of the AC/BP/ZnO composite, cyclic photocatalytic degradation experiments were performed using Direct Red 80 (DR80) degradation under visible light. The

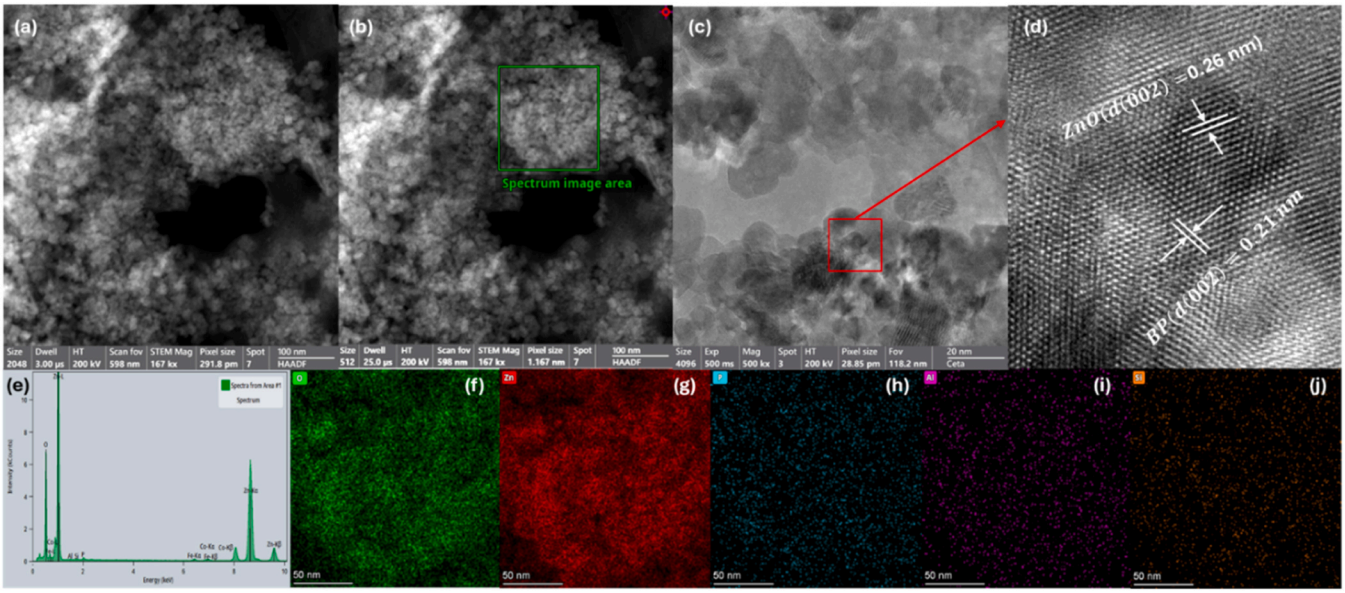

Fig. 6. STEM-EDX and HRTEM images of AC/BP/ZnO composite: (a–b) STEM images, (c–d) HRTEM images, (e) EDX spectrum, (f to j) elemental mapping of O, Zn, P, Al, and Si.

composite was recovered after each cycle by centrifugation, washed with Milli-Q water, dried at 100°C, and reused under identical conditions (1 g/L catalyst, 20 mg/L DR80, 8 h illumination per cycle). As shown in Fig. 8, the overall removal efficiency (adsorption + photodegradation) remained consistently high, achieving 92 % after 8 h in the fifth cycle, nearly identical to the 93 % observed in the first cycle. This negligible variation in performance across five cycles demonstrates the exceptional durability and stability of the AC/BP/ZnO composite as a photocatalyst. The robust performance is attributed to the strong interfacial interactions between ZnO, BP, and the activated kaolinite matrix, which prevent nanoparticle aggregation and Zn^{2+} leaching, as confirmed by post-cycling ICP-OES analysis showing minimal Zn^{2+} release. The high surface area and adsorption capacity of the clay matrix further contribute to maintaining active site accessibility, ensuring sustained photocatalytic efficiency. These findings highlight the potential of the AC/BP/ZnO composite as a sustainable, scalable photocatalyst for wastewater treatment, particularly for industrial applications leveraging low-cost, abundant kaolinite.

To elucidate the charge transfer mechanism and identify the primary reactive species involved in the photocatalytic degradation of Direct Red 80 (DR80) by the AC/BP/ZnO composite, scavenger experiments were conducted using benzoquinone (BQ), isopropanol (IPA), and triethanolamine (TEOA) to selectively trap superoxide radicals ($\cdot O_2^-$), hydroxyl radicals (·OH), and photogenerated holes (h^+), respectively [54]. The experiments were performed under visible light irradiation (1 g/L catalyst, 20 mg/L DR80, 2 h illumination), with scavenger concentrations (1 mmol) optimized to ensure selective quenching without altering the system's pH or stability. As shown in Fig. 10, the addition of scavengers led to a reduction in the DR80 degradation efficiency compared to the control experiment (65 % removal without scavengers). Specifically, the degradation efficiency decreased by 18 % with BQ, 7 % with IPA, and 10 % with TEOA, resulting in removal efficiencies of 47 %, 58 %, and 55 %, respectively. These results indicate that superoxide radicals ($\cdot O_2^-$) play a predominant role in the photocatalytic degradation process, followed by hydroxyl radicals (·OH) and photogenerated holes (h^+), the latter still contributing significantly to the reaction. The pronounced effect of BQ suggests that $\cdot O_2^-$ radicals, generated via the reduction of dissolved oxygen by photogenerated electrons in the conduction band of ZnO or BP, are the primary reactive species driving dye degradation. The moderate impact of TEOA highlights the role of h^+ in direct oxidation or in generating additional reactive oxygen species (ROS) at the composite surface. The lesser influence of IPA indicates that ·OH radicals, while active, are less critical in this system, possibly due to the preferential formation of $\cdot O_2^-$ under visible light. These findings confirm an efficient charge separation in the AC/BP/ZnO heterostructure, where the activated clay and BP facilitate electron transfer to oxygen molecules, while the ZnO/BP interface enhances hole migration to the surface for oxidation reactions [48]. The synergy between the high adsorption capacity of the clay matrix and the charge transfer properties of BP and ZnO underpins the composite's superior photocatalytic performance, as evidenced by the sustained activity of all reactive species.

A mechanistic scheme is proposed in Fig. 10 for dye degradation over AC/BP/ZnO.

Upon visible-light absorption, electrons (e^-) are excited from the ZnO valence band (VB) to the conduction band (CB), leaving behind holes (h^+) in the VB. The negatively charged AC/BP matrix, onto which ZnO is immobilized, facilitates hole migration by electrostatic attraction, enhancing charge separation due to surface passivation [84,85].

Photogenerated electrons on the ZnO surface reduce dissolved oxygen to generate reactive oxygen species (ROS), while h^+ on AC/BP also contribute to ROS generation. These highly reactive radicals initiate oxidative degradation of azo dye molecules.

Additionally, the clay's high adsorption capacity ensures close proximity between dyes and active sites, increasing the likelihood of ROS–pollutant interactions. This synergistic effect between adsorption and interfacial charge transfer accounts for the superior photocatalytic performance observed in PL and kinetic studies.

In line with recent advancements in ZnO-based heterostructured photocatalysts, the superior performance of the AC/BP/ZnO composite can be contextualized within broader trends in photocatalytic systems designed for pollutant degradation and H_2 evolution. A comprehensive review in [86] highlights the progress in ZnO heterostructures, emphasizing the role of interfacial engineering in overcoming limitations such as rapid charge recombination and limited visible-light absorption, which aligns with the enhanced charge separation observed in our BP-doped clay-supported ZnO system. Similarly, the S-scheme Nb_2O_5/La_2O_3 heterojunction reported in [87] achieves a 14.5-fold improvement in H_2 production under simulated sunlight, attributed to preserved redox potentials and efficient electron transfer—principles

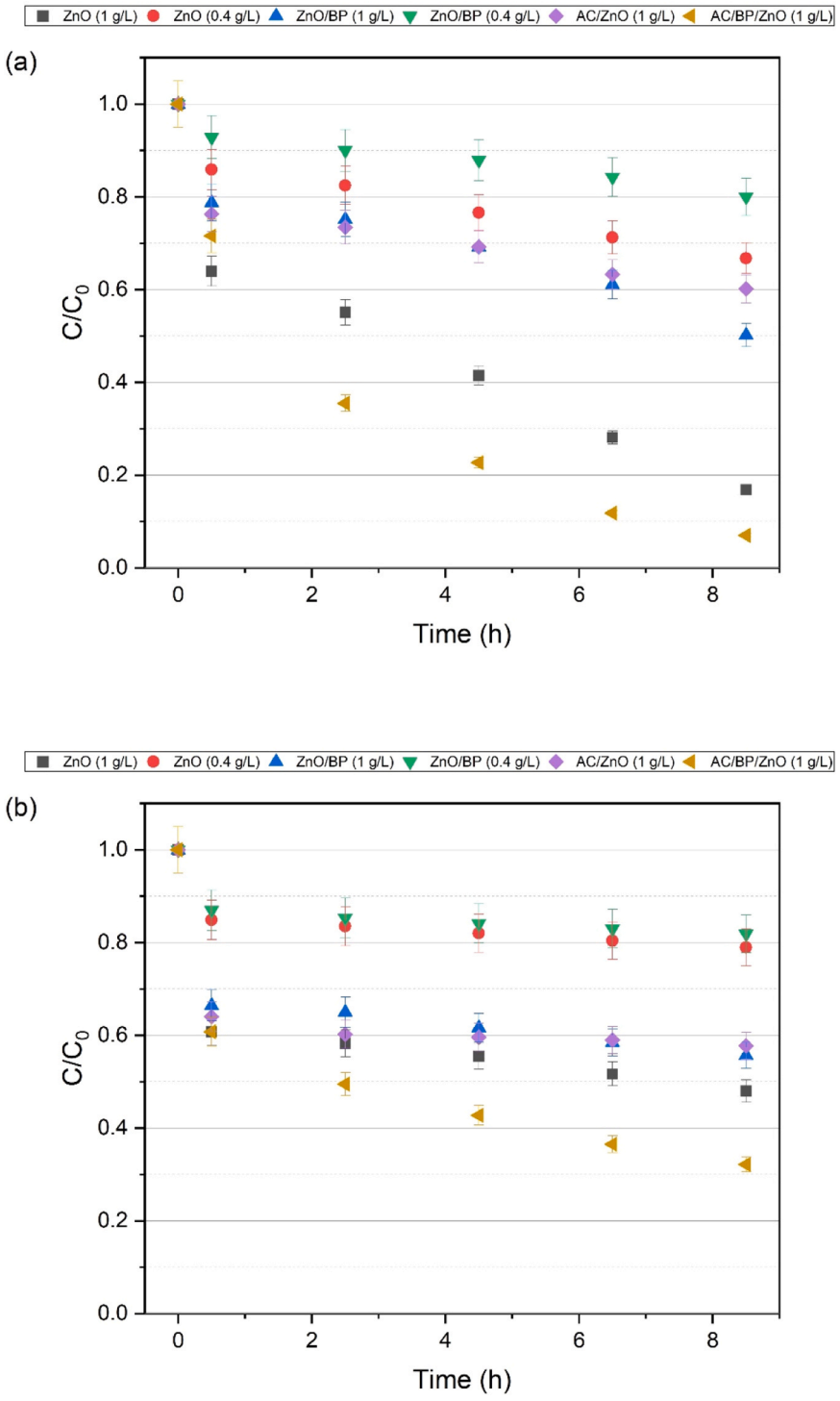

Fig. 7. Photodegradation curves of (a) DR80 and (b) DB1 under visible light.

Table 3
First-order rate constants for visible-light degradation of DR80 and DB1.

Samples	k_{DR80} (h^{-1})	k_{DB1} (h^{-1})
ZnO (1 g/L)	0.147	0.028
ZnO (0.4 g/L)	0.031	0.009
ZnO/BP (1 g/L)	0.048	0.021
ZnO/BP (0.4 g/L)	0.017	0.008
AC/ZnO (1 g/L)	0.029	0.015
AC/BP/ZnO (1 g/L)	0.295	0.083

that mirror the synergistic effects in AC/BP/ZnO, where BP acts as a conductive bridge to extend charge carrier lifetimes. Furthermore, Sr-doped ZnO/CNTs nanocomposites, as demonstrated in [88], exhibit a 33.7-fold increase in H_2 evolution rate due to doping-induced defects and CNT-mediated charge transport, providing a comparative benchmark for the stability and recyclability of our composite, which maintains over 92 % efficiency after five cycles. Finally, the Cu-mediated Z-scheme ZnO–Cu–CdS system in [89] delivers multifunctional performance, including 97 % methylene blue degradation and 5579 μmol h^{-1} g^{-1} H_2 evolution, underscoring the efficacy of metal-mediated heterojunctions in promoting redox reactions, akin to the interfacial

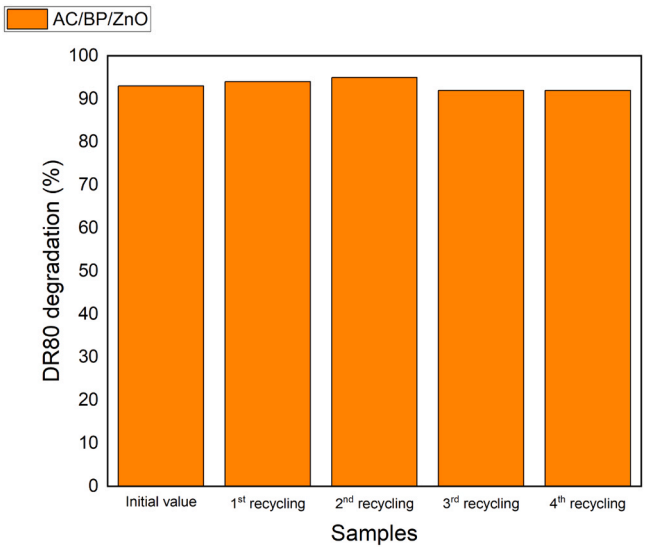

Fig. 8. DR80 degradation under visible light for 5 successive photocatalytic tests (5 ×8 h of illumination); the values correspond to the DR80 degradation values measured after 8 h of degradation in each of the 5 experiments under visible light for the AC/BP/ZnO composite sample.

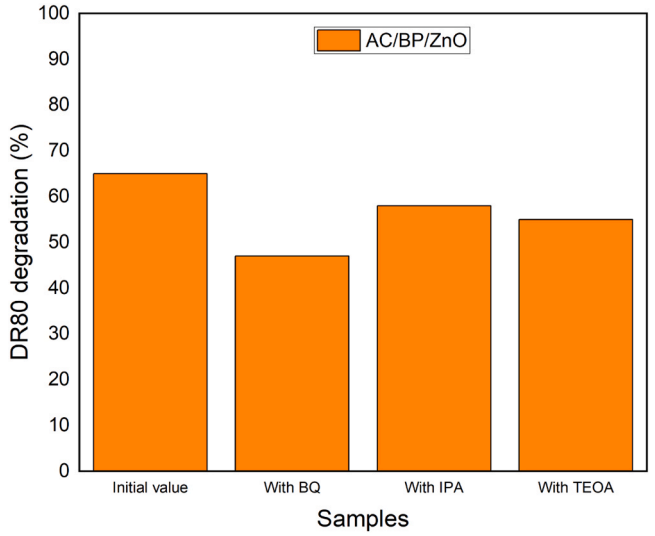

Fig. 9. Photocatalytic degradation of DR80 under visible light in the presence of scavengers (BQ, IPA, TEOA) for the AC/BP/ZnO composite, compared to the control initial value (no scavenger). The values represent the DR80 removal efficiencies after 2 h of illumination.

interactions in AC/BP/ZnO that facilitate ROS generation and dye degradation. These studies collectively reinforce the potential of hybrid ZnO-based systems for scalable, sustainable photocatalysis, positioning our AC/BP/ZnO composite as a promising candidate for wastewater treatment and energy applications.

4. Conclusions

In this work, we successfully synthesized a novel ternary photocatalyst based on black phosphorus-modified activated clay (AC/BP) decorated with ZnO nanoparticles, using a combination of solvothermal synthesis in ethylenediamine, co-precipitation, and the valorization of natural Cameroonian kaolinite. The wurtzite-phase ZnO nanoparticles were effectively immobilized on the BP-modified clay surface, resulting in a stable heterostructured composite.

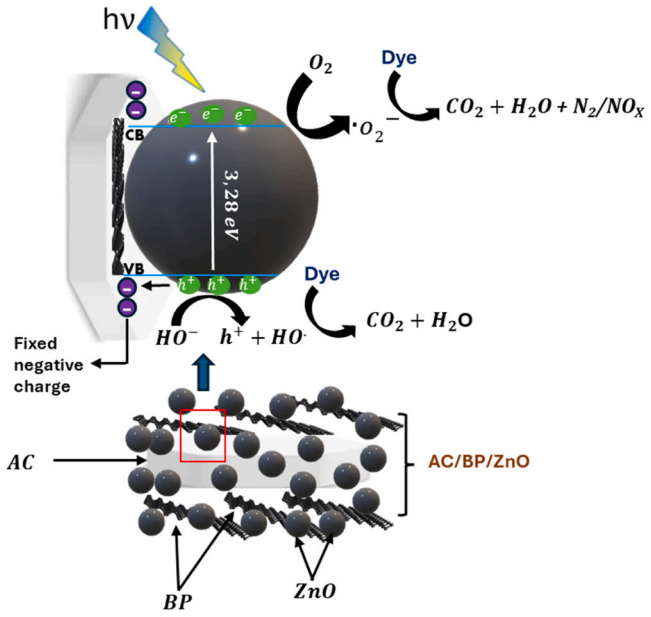

Fig. 10. Schematic of the photocatalytic degradation mechanism over AC/BP/ZnO.

Comprehensive characterization revealed that the microstructure, light absorption capacity, and photocatalytic performance of the composites varied depending on the material composition and the presence of BP. The introduction of black phosphorus and its interfacial interaction with both ZnO and the clay matrix played a key role in enhancing the material's photoactivity.

Among all tested materials, the AC/BP/ZnO composite demonstrated the best photocatalytic performance, with degradation rates for the two model dyes, DR80 and DB1, being approximately 2 and 3 times faster, respectively, compared to pure ZnO under visible-light irradiation. This improvement is attributed to the synergistic interfacial effects arising from: (i) the controlled immobilization of ZnO nanocrystals bearing oxygen and zinc vacancy defects, and (ii) the use of a BP-doped activated clay matrix, which serves both as an adsorbent and an electron mediator.

These interfacial interactions promoted efficient charge separation, as evidenced by photoluminescence analysis, and enhanced both the adsorption of dye molecules and the photocatalytic degradation mechanism. The results suggest that such clay-based heterostructures combining 2D BP and 3D ZnO offer a promising and sustainable platform for visible-light-driven photocatalysis in water treatment applications.

This work also highlights the potential of underutilized natural resources, such as Cameroonian kaolinite, as low-cost and abundant supports for advanced photocatalysts. The synthesis strategy employed is compatible with scalable and environmentally friendly processes, paving the way for sustainable applications in water remediation.

CRediT authorship contribution statement

Pierre Ngue Song: conceptualization, methodology, formal analysis, investigation, writing – original draft, writing – review & editing. Stéphanie D. Lambert: methodology, formal analysis, writing – review & editing, funding acquisition, and project administration. Antoine Farcy: investigation, formal analysis, and writing – review & editing. Abdelhalim Ouhaibi: investigation, formal analysis, and writing – review & editing. Louise Lejeune: investigation, formal analysis, and writing – review & editing. Pierre Eloy: investigation, formal analysis, and writing – review & editing. Sophie Hermans: investigation, formal analysis, and writing – review & editing. Maxime Delaey: investigation, formal

analysis, and writing – review & editing. Dirk Poelmans: investigation, formal analysis, and writing – review & editing. Julien G. Mahy: conceptualization, methodology, formal analysis, investigation, writing – original draft, writing – review & editing, and supervision.

Declaration of Competing Interest

The authors declare that there are no conflicts of interest concerning this work.

Acknowledgments

S.D.L. thanks the F.R.S.-FNRS for her Researcher Director position.

Data Availability

The raw/processed data required to reproduce these findings can be shared on demand.

References

[1] M.L. Catarino, F. Sampaio, A.L. Gonçalves, Sustainable wet processing technologies for the textile industry: a comprehensive review, Sustain. (Switz.) 17 (2025), https://doi.org/10.3390/su17073041.
[2] S. Maiti, M. Shahid, R.V. Adivarekar, Sustainable Coloration Techniques in Textiles, Springer Nature Singapore, 2025, https://doi.org/10.1007/978-981-96-4975-4.
[3] D.A. Yaseen, M. Scholz, Textile dye wastewater characteristics and constituents of synthetic effluents: a critical review, Int. J. Environ. Sci. Technol. 16 (2019) 1193–1226, https://doi.org/10.1007/s13762-018-2130-z.
[4] P. Ngue Song, J.G. Mahy, A. Farcy, C. Calberg, N. Fagel, S.D. Lambert, Development of novel composite materials based on kaolinitic clay modified with ZnO for the elimination of azo dyes by adsorption in water, Results Surf. Interfaces 16 (2024), https://doi.org/10.1016/j.rsurfi.2024.100255.
[5] M. Roy, V.K. Pathak, R. Sharma, Policies and legislative framework for industrial wastewater management. Integrated Biotechnological Solutions for the Treatment of Industrial Wastewater, Elsevier, 2025, pp. 527–557, https://doi.org/10.1016/b978-0-443-23607-5.00009-x.
[6] M.D.N. Ramos, C.S. Santana, C.C.V. Velloso, A.H.M. da Silva, F. Magalhães, A. Aguiar, A review on the treatment of textile industry effluents through Fenton processes, Process Saf. Environ. Prot. 155 (2021) 366–386, https://doi.org/10.1016/j.psep.2021.09.029.
[7] A. Yadav, S. Mukherji, A. Garg, Removal of chemical oxygen demand and color from simulated textile wastewater using a combination of chemical/physicochemical processes, Ind. Eng. Chem. Res 52 (2013) 10063–10071, https://doi.org/10.1021/ie400855b.
[8] P. Hoel, A.R. Moreno, D. Bianchi, Mechanisms controlling lower trophic ecosystem response to ocean outfall discharges: role of nitrogen form and freshwater volume, Reg. Stud. Mar. Sci. 78 (2024), https://doi.org/10.1016/j.rsma.2024.103739.
[9] K.F. Ngulube, A. Abdelhaleem, A.I. Osman, L. Peng, M. Nasr, Advancing sustainable water treatment strategies: harnessing magnetite-based photocatalysts and techno-economic analysis for enhanced wastewater management in the context of SDGs, Environ. Sci. Pollut. Res. (2024), https://doi.org/10.1007/s11356-024-32680-9.
[10] A.C.R. Ngo, D. Tischler, Microbial degradation of azo dyes: approaches and prospects for a hazard-free conversion by microorganisms, Int J. Environ. Res Public Health 19 (2022), https://doi.org/10.3390/ijerph19084740.
[11] Md.M. Islam, A.R. Aidid, J.N. Mohshin, H. Mondal, S. Ganguli, A.K. Chakraborty, A critical review on textile dye-containing wastewater: ecotoxicity, health risks, and remediation strategies for environmental safety, Clean. Chem. Eng. 11 (2025) 100165, https://doi.org/10.1016/j.clce.2025.100165.
[12] J.I. Mnyango, B. Nyoni, C. Phiri, B.G. Fouda-Mbanga, S.O. Amusat, A. Maringa, B. Yalala-Ndlovu, B. Hlabano-Moyo, Z. Tywabi-Ngeva, S.P. Hlangothi, Sustainable wastewater treatment: mechanistic, environmental, and economic insights into biochar for synthetic dye removal, Materials 9 (2025), https://doi.org/10.1016/j.nxmate.2025.100974.
[13] J.O. Tijani, O.O. Fatoba, G. Madzivire, L.F. Petrik, A review of combined advanced oxidation technologies for the removal of organic pollutants from water, Water Air Soil Pollut. 225 (2014), https://doi.org/10.1007/s11270-014-2102-y.
[14] A. Chakravorty, S. Roy, A review of photocatalysis, basic principles, processes, and materials, Sustain. Chem. Environ. 8 (2024), https://doi.org/10.1016/j.scenv.2024.100155.
[15] B. Zhou, Z. Zheng, T. Zhao, X. Huang, X. Wu, Kinetics and mechanisms for the degradation of pharmaceutical and personal care product pollutants in the process of electrochemistry-driven in-situ chlorination coupled with solar photocatalysis, J. Water Process Eng. 67 (2024), https://doi.org/10.1016/j.jwpe.2024.106281.
[16] A.F. Gouveia, G.C. de Assis, L.K. Ribeiro, L.H. Mascaro, M. Calatayud, A.C.S. C. Teixeira, Heterogeneous photocatalysis as an efficient process for degrading MPs/ NPs in aqueous media: a systematic review, J. Environ. Chem. Eng. 13 (2025), https://doi.org/10.1016/j.jece.2025.117878.
[17] S.N. Tan, M.L. Yuen, R.A. Ramli, Photocatalysis of dyes: operational parameters, mechanisms, and degradation pathway, Green. Anal. Chem. 12 (2025), https://doi.org/10.1016/j.greeac.2025.100230.
[18] I. Grčić, G. Li Puma, Photocatalytic degradation of water contaminants in multiple photoreactors and evaluation of reaction kinetic constants independent of photon absorption, irradiance, reactor geometry, and hydrodynamics, Environ. Sci. Technol. 47 (2013) 13702–13711, https://doi.org/10.1021/es403472e.
[19] A. Mancuso, G. Iervolino, Synthesis and application of innovative and environmentally friendly photocatalysts: a review, Catalysts 12 (2022), https://doi.org/10.3390/catal12101074.
[20] J.G. Mahy, C. Wolfs, C. Vreuls, S. Drot, S. Dircks, A. Boergers, J. Tuerk, S. Hermans, S.D. Lambert, Advanced oxidation processes for waste water treatment: from lab-scale model water to on-site real waste water, Environ. Technol. (U. Kingd.) 42 (2021) 3974–3986, https://doi.org/10.1080/09593330.2020.1797894.
[21] D.F. Ollis, E. Pelizzetti, N. Serpone, Destruction of water contaminants, Environ. Sci. Technol. 25 (1991) 1522–1529, https://doi.org/10.1021/es00021a001.
[22] A.A. Ansari, R. Lv, S. Gai, A.K. Parchur, P.R. Solanki, Archana, Z.A. Ansari, M. Dhayal, P. Yang, M.K. Nazeeruddin, M.M. Tavakoli, ZnO nanostructures – Future frontiers in photocatalysis, solar cells, sensing, supercapacitor, fingerprint technologies, toxicity, and clinical diagnostics, Coord. Chem. Rev. 515 (2024), https://doi.org/10.1016/j.ccr.2024.215942.
[23] Ü. Özgür, Y.I. Alivov, C. Liu, A. Teke, M.A. Reshchikov, S. Doğan, V. Avrutin, S. J. Cho, H. Morkç, A comprehensive review of ZnO materials and devices, J. Appl. Phys. 98 (2005) 1–103, https://doi.org/10.1063/1.1992666.
[24] A. Farcy, J.G. Mahy, C. Alié, J. Caucheteux, D. Poelman, Z. Yang, P. Eloy, N. Body, S. Hermans, B. Heinrichs, S.D. Lambert, Kinetic study of p-nitrophenol degradation with zinc oxide nanoparticles prepared by sol–gel methods, J. Photochem. Photobio. A Chem. 456 (2024), https://doi.org/10.1016/j.jphotochem.2024.115804.
[25] X. Li, M. Li, J. Yang, X. Li, T. Hu, J. Wang, Y. Sui, X. Wu, L. Kong, Synergistic effect of efficient adsorption g-C3N4/ZnO composite for photocatalytic property, J. Phys. Chem. Solids 75 (2014) 441–446, https://doi.org/10.1016/j.jpcs.2013.12.001.
[26] B. Abebe, H.C.A. Murthy, E. Amare, Enhancing the photocatalytic efficiency of ZnO: Defects, heterojunction, and optimization, Environ. Nanotechnol. Monit. Manag 14 (2020), https://doi.org/10.1016/j.enmm.2020.100336.
[27] J.Sen Chang, M.N. Chong, P.E. Poh, J.D. Ocon, M.Z.H. Md Zoqratt, S.M. Lee, Impacts of morphological-controlled ZnO nanoarchitectures on aerobic microbial communities during real wastewater treatment in an aerobic-photocatalytic system, Environ. Pollut. 259 (2020), https://doi.org/10.1016/j.envpol.2019.113867.
[28] A.U. Ammar, F. Bakan-Misirlioglu, M.H. Aleinawi, G. Franzo, G.G. Condorelli, F.N. T. Yesilbag, Y.O. Yesilbag, S. Mirabella, E. Erdem, All-in-one supercapacitors with high performance enabled by Mn/Cu doped ZnO and MXene, Mater. Res Bull. 165 (2023), https://doi.org/10.1016/j.materresbull.2023.112334.
[29] M. Chauhan, V.K. Saini, S. Suthar, Ti-pillared montmorillonite clay for adsorptive removal of amoxicillin, imipramine, diclofenac-sodium, and paracetamol from water, J. Hazard Mater. 399 (2020), https://doi.org/10.1016/j.jhazmat.2020.122832.
[30] M. Zarei, N. Jesarati, E. Narimani, M. Darbandi, R. Torkamani, B. Aslibeiki, Fe-doped ZnO nanoparticles prepared by high energy ball milling with enhanced sonophotocatalytic performance, Adv. Powder Technol. 35 (2024), https://doi.org/10.1016/j.apt.2024.104550.
[31] K. SenthilKannan, U. Chinnaiyan, K. Suganya, V. Raghuraman, S. Partheepan, Photo catalytic, anti bacterial activities of Ce doped zinc oxide nano particles, in: Mater Today Proc, Elsevier Ltd, 2020, pp. 2753–2755, https://doi.org/10.1016/j.matpr.2020.01.576.
[32] U. Mahanta, M. Khandelwal, A.S. Deshpande, TiO2@SiO2 nanoparticles for methylene blue removal and photocatalytic degradation under natural sunlight and low-power UV light, Appl. Surf. Sci. 576 (2022), https://doi.org/10.1016/j.apsusc.2021.151745.
[33] A.G. Abd-Elrahim, D.M. Chun, Room-temperature deposition of ZnO-graphene nanocomposite hybrid photocatalysts for improved visible-light-driven degradation of methylene blue, Ceram. Int 47 (2021) 12812–12825, https://doi.org/10.1016/j.ceramint.2021.01.142.
[34] A. Chatterjee, R. Thanneeru, A. Saha, K.K. Guthikonda, Photodegradation of toxic malachite green dye by ZnO and ZnO/SiO2 nanocomposites under solar radiation: a green practice, Chem. Pap. 78 (2024) 2301–2311, https://doi.org/10.1007/s11696-023-03238-9.
[35] A.D. Go, F.M. dela Rosa, D.H. Camacho, E.R. Punzalan, Photocatalytic degradation of levofloxacin using ZnO/hydroxyapatite nanocomposite: optimization using response surface methodology, Chem. Data Collect. 50 (2024), https://doi.org/10.1016/j.cdc.2024.101126.
[36] M.H.T. Mbognou, S.D. Lambert, J. Caucheteux, A. Farcy, C. Alié, N. Fagel, E. D. Woumfo, J.G. Mahy, Hybrid clay-based materials for organic dyes and pesticides elimination in water, J. Solgel Sci. Technol. 105 (2023) 461–470, https://doi.org/10.1007/s10971-022-06005-6.
[37] H. Benhebal, C. Wolfs, S. Kadi, R.G. Tilkin, B. Allouche, D. Lambert, J.G. Mahy, Visible light sensitive SnO2/ZnCo2O4 material for the photocatalytic removal of organic pollutants in water, Inorg. (Basel) 7 (2019) 77.
[38] S. Douven, J.G. Mahy, C. Wolfs, C. Reyserhove, D. Poelman, F. Devred, E. M. Gaigneaux, S.D. Lambert, Efficient N, Fe Co-doped TiO2 active under cost-effective visible LED light: From powders to films, Catalysts 10 (2020), https://doi.org/10.3390/catal10050547.
[39] E. Pakdel, W.A. Daoud, S. Seyedin, J. Wang, J.M. Razal, L. Sun, X. Wang, Tunable photocatalytic selectivity of TiO2/SiO2 nanocomposites: effect of silica and

isolation approach, Colloids Surf. A Physicochem Eng. Asp. 552 (2018) 130–141, https://doi.org/10.1016/j.colsurfa.2018.04.070.
[40] U.I. Gaya, A.H. Abdullah, Heterogeneous photocatalytic degradation of organic contaminants over titanium dioxide: a review of fundamentals, progress and problems, J. Photochem. Photobiol. C Photochem. Rev. 9 (2008) 1–12, https://doi.org/10.1016/j.jphotochemrev.2007.12.003.
[41] N. Yahya, F. Aziz, N.A. Jamaludin, M. A. Mutalib, A.F. Ismail, W.N. Salleh, J. Jaafar, N. Yusof, N. A. Ludin, A review of integrated photocatalyst adsorbents for wastewater treatment, J. Environ. Chem. Eng. 6 (2018) 7411–7425, https://doi.org/10.1016/j.jece.2018.06.051.
[42] J.G. Mahy, M.H.T. Mbognou, C. Léonard, N. Fagel, E.D. Woumfo, S.D. Lambert, Natural clay modified with ZnO/TiO2 to enhance pollutant removal from water, Catalysts 12 (2022), https://doi.org/10.3390/catal12020148.
[43] J. Liu, X. Qu, C. Zhang, W. Dong, C. Fu, J. Wang, Q. Zhang, High-yield aqueous synthesis of partial-oxidized black phosphorus as layered nanodot photocatalysts for efficient visible-light driven degradation of emerging organic contaminants, J. Clean. Prod. 377 (2022), https://doi.org/10.1016/j.jclepro.2022.134228.
[44] S. Zhu, Q. Liang, Y. Xu, H. Fu, X. Xiao, Facile solvothermal synthesis of black phosphorus nanosheets from red phosphorus for efficient photocatalytic hydrogen evolution, Eur. J. Inorg. Chem. 2020 (2020) 773–779, https://doi.org/10.1002/ejic.202000048.
[45] J.R. Brent, N. Savjani, E.A. Lewis, S.J. Haigh, D.J. Lewis, P. O'Brien, Production of few-layer phosphorene by liquid exfoliation of black phosphorus, Chem. Commun. 50 (2014) 13338–13341, https://doi.org/10.1039/c4cc05752j.
[46] R.K. Mishra, J. Sarkar, I. Chianella, S. Goel, H.Y. Nezhad, Black phosphorus: the rise of phosphorene in 2D materials applications, Materials 4 (2024), https://doi.org/10.1016/j.nxmate.2024.100217.
[47] K.S. Mohammed, M. Atlabachew, G.W. Derbie, B.A. Berhie, Nano modified kaolin-based materials and their application: a review, JCIS Open 20 (2025), https://doi.org/10.1016/j.jciso.2025.100153.
[48] H. Zhao, J. Yang, Z. Zhang, L. Yang, F. Song, E. Zhang, J. Wang, Q. Zhang, Y. Liu, J. An, Z. Meng, Network of graphene/black phosphorus/ZnO for enhanced photocatalytic dye removal under visible light, Mater. Chem. Phys. 295 (2023), https://doi.org/10.1016/j.matchemphys.2022.127138.
[49] S.A. Ansari, Elemental semiconductor red phosphorus/ZnO nanohybrids as high performance photocatalysts, Ceram. Int 49 (2023) 17746–17752, https://doi.org/10.1016/j.ceramint.2023.02.140.
[50] S. Moradian, G. Mohammadi Ziarani, A. Badiei, S. Iravani, ZnO/black phosphorus/C3N4 composite: an effective photocatalyst for Cr (VI) reduction and degradation of rhodamine B, Environ. Res 238 (2023), https://doi.org/10.1016/j.envres.2023.117122.
[51] P.N. Song, J.G. Mahy, C. Calberg, A. Farcy, J. Caucheteux, N. Fagel, S.D. Lambert, Influence of thermal and acidic treatments on the morphology of a natural kaolinitic clay mineral, Results Surf. Interfaces 12 (2023), https://doi.org/10.1016/j.rsurfi.2023.100131.
[52] J.G. Mahy, S.D. Lambert, G.L.M. Léonard, A. Zubiaur, P.Y. Olu, A. Mahmoud, F. Boschini, B. Heinrichs, Towards a large scale aqueous sol-gel synthesis of doped TiO2: study of various metallic dopings for the photocatalytic degradation of p-nitrophenol, J. Photochem. Photobio. A Chem. 329 (2016) 189–202, https://doi.org/10.1016/j.jphotochem.2016.06.029.
[53] C.M. Malengreaux, S. Douven, D. Poelman, B. Heinrichs, J.R. Bartlett, An ambient temperature aqueous sol–gel processing of efficient nanocrystalline doped TiO2-based photocatalysts for the degradation of organic pollutants, J. Solgel Sci. Technol. 71 (2014) 557–570, https://doi.org/10.1007/s10971-014-3405-6.
[54] Z. Ye, J. Li, M. Zhou, H. Wang, Y. Ma, P. Huo, L. Yu, Y. Yan, Well-dispersed nebula-like ZnO/CeO2@HNTs heterostructure for efficient photocatalytic degradation of tetracycline, Chem. Eng. J. 304 (2016) 917–933, https://doi.org/10.1016/j.cej.2016.07.014.
[55] W.A. Freitas, B.E.C.F. Soares, M.S. Rodrigues, P. Trigueiro, L.M.C. Honorio, R. Peña-Garcia, A.C.S. Alcântara, E.C. Silva-Filho, M.G. Fonseca, M.B. Furtini, J. A. Osajima, Facile synthesis of ZnO-clay minerals composites using an ultrasonic approach for photocatalytic performance, J. Photochem. Photobio. A Chem. 429 (2022), https://doi.org/10.1016/j.jphotochem.2022.113934.
[56] R. Álvarez-Chimal, V.I. García-Pérez, M.A. Álvarez-Pérez, R. Tavera-Hernández, L. Reyes-Carmona, M. Martínez-Hernández, J.Á. Arenas-Alatorre, Influence of the particle size on the antibacterial activity of green synthesized zinc oxide nanoparticles using Dysphania ambrosioides extract, supported by molecular docking analysis, Arab. J. Chem. 15 (2022), https://doi.org/10.1016/j.arabjc.2022.103804.
[57] R. Djefaflia, D. Lerari, K. Bachari, Covid-19 and nanoform zinc oxide interaction: a forcite module of materials studio software study, Clay Res. 38 (2019) 43–55, https://doi.org/10.5958/0974-4509.2019.00001.9.
[58] H. Shaikh, R. Saleem, I.A. Halepoto, M.S. Barhaam, M.Y. Soomro, M.A. Abbasi, N. M. Shaikh, M.A. Bhatti, S.H. Wassan, E. Dawi, A. Tahira, M. Tonezzer, Z. H. Ibupoto, Facile and low-cost fabrication of ZnO/kaolinite composites by modifying the kaolinite composition for efficient degradation of methylene blue under sunlight illumination, Catalysts 15 (2025), https://doi.org/10.3390/catal15060566.
[59] M.H. Suhag, A. Khatun, I. Tateishi, M. Furukawa, H. Katsumata, S. Kaneco, One-step fabrication of the ZnO/g-C3N4 composite for visible light-responsive photocatalytic degradation of bisphenol E in aqueous solution, ACS Omega 8 (2023) 11824–11836, https://doi.org/10.1021/acsomega.2c06678.
[60] M. Lahbib, C. Mejri, M. Bejaoui, A. Oueslati, W. Oueslati, Hybrid nanocomposite design: exploring the interplay between microstructure, dielectric properties, and photocatalytic activities in Chitosan/Na-Montmorillonite/Fe3O4 nanoparticles, Emergent Mater. (2025), https://doi.org/10.1007/s42247-025-01046-3.
[61] D.R. Paul, S. Gautam, P. Panchal, S.P. Nehra, P. Choudhary, A. Sharma, ZnO-Modified g-C3N4: a potential photocatalyst for environmental application, ACS Omega 5 (2020) 3828–3838, https://doi.org/10.1021/acsomega.9b02688.
[62] A.K. Avornyo, S.W. Hasan, F. Banat, C.V. Chrysikopoulos, Preparation, characterization, and applications of kaolin/kaolin-based composite membranes in oily wastewater treatment: recent developments, challenges, and opportunities, J. Environ. Manag. 370 (2024), https://doi.org/10.1016/j.jenvman.2024.122800.
[63] J. Jiang, Y. Wang, J. Wu, H. Wang, Arramel, Y. Zou, J. Zou, H. Wang, Charge transfer interfaces across black phosphorus/Co, N Co-doped carbon heterojunction for enhanced electrocatalytic water splitting, J. Mater. Sci. Technol. 178 (2024) 171–178, https://doi.org/10.1016/j.jmst.2023.09.009.
[64] H.L. Guo, Q. Zhu, X.L. Wu, Y.F. Jiang, X. Xie, A.W. Xu, Oxygen deficient ZnO1-x nanosheets with high visible light photocatalytic activity, Nanoscale 7 (2015) 7216–7223, https://doi.org/10.1039/c5nr00271k.
[65] J. Zhang, Y. Dong, J. Yao, M. Zhai, M. Zhu, G. Wang, J. Li, P.F. Ferrari, P. Perego, B. Liu, Copper doping and oxygen vacancy synergistic modification of zinc oxide nanosheets: significantly improved antibacterial properties, Mater. Lett. 369 (2024), https://doi.org/10.1016/j.matlet.2024.136777.
[66] H. Yu, H. Xu, T. Hao, Y. Yuan, B. Zhang, H. Wang, G. Shao, B. Fan, H. Lu, Facile synthesis of ZnO/halloysite nanotube composite with greatly enhanced photocatalytic performance, Colloids Surf. A Physicochem Eng. Asp. 688 (2024), https://doi.org/10.1016/j.colsurfa.2024.133633.
[67] J.D. Wood, S.A. Wells, D. Jariwala, K.S. Chen, E. Cho, V.K. Sangwan, X. Liu, L. J. Lauhon, T.J. Marks, M.C. Hersam, Effective passivation of exfoliated black phosphorus transistors against ambient degradation, Nano Lett. 14 (2014) 6964–6970, https://doi.org/10.1021/nl5032293.
[68] R. Chanson, S. Bouchoule, C. Cardinaud, C. Petit-Etienne, E. Cambril, A. Rhallabi, S. Guilet, E. Blanquet, X-ray photoelectron spectroscopy analysis of the effect of temperature upon surface composition of InP etched in Cl2-based inductively coupled plasma, J. Vac. Sci. Technol. B Nanotechnol. Microelectron. Mater. Proc. Meas. Phenom. 32 (2014), https://doi.org/10.1116/1.4862256.
[69] Q. Li, Y. Cen, J. Huang, X. Li, H. Zhang, Y. Geng, B.I. Yakobson, Y. Du, X. Tian, Zinc oxide-black phosphorus composites for ultrasensitive nitrogen dioxide sensing, Nanoscale Horiz. 3 (2018) 525–531, https://doi.org/10.1039/c8nh00052b.
[70] H. Uk Lee, S.C. Lee, J. Won, B.C. Son, S. Choi, Y. Kim, S.Y. Park, H.S. Kim, Y.C. Lee, J. Lee, Stable semiconductor black phosphorus (BP)@titanium dioxide (TiO2) hybrid photocatalysts, Sci. Rep. 5 (2015), https://doi.org/10.1038/srep08691.
[71] K. Phongarthit, P. Amornpitoksuk, S. Suwanboon, Synthesis, characterization, and photocatalytic properties of zno nanoparticles prepared by a precipitation-calcination method using a natural alkaline solution, Mater. Res Express 6 (2019), https://doi.org/10.1088/2053-1591/aaf8db.
[72] Z. Huang, L. Li, Z. Li, H. Li, J. Wu, Synthesis of novel kaolin-supported g-C3N4/CeO2. Composites with enhanced photocatalytic removal of ciprofloxacin, Materials 13 (2020), https://doi.org/10.3390/MA13173811.
[73] J.T. Kloprogge, Spectroscopic Methods in the Study of Kaolin Minerals and Their Modifications, Springer, 2019. ⟨http://www.springer.com/series/13488⟩.
[74] M. Zhou, D. Han, X. Liu, C. Ma, H. Wang, Y. Tang, P. Huo, W. Shi, Y. Yan, J. Yang, Enhanced visible light photocatalytic activity of alkaline earth metal ions-doped CdSe/rGO photocatalysts synthesized by hydrothermal method, Appl. Catal. B 172–173 (2015) 174–184, https://doi.org/10.1016/j.apcatb.2015.01.004.
[75] J. Singh, G.P. Singh, K.J. Singh, N. Virdi, D.A. Tonpe, R.C. Singh, Ball mill synthesized Fe/ZnO nanostructures for dye degradation, heavy metal extraction and light emission applications: Experimental and DFT Perspectives, Desalin. Water Treat. 322 (2025), https://doi.org/10.1016/j.dwt.2025.101155.
[76] F. Hussin, H.O. Lintang, S.L. Lee, L. Yuliati, Photocatalytic synthesis of reduced graphene oxide-zinc oxide: Effects of light intensity and exposure time, J. Photochem. Photobio. A Chem. 340 (2017) 128–135, https://doi.org/10.1016/j.jphotochem.2017.03.016.
[77] T.P. Nguyen, H.P. Dang, L.G. Nguyen, C.D. Le, Synthesis of ZnO nanoparticles-based fluorescent ink for information encryption and security applications, Opt. Mater. (Amst.) 157 (2024), https://doi.org/10.1016/j.optmat.2024.116296.
[78] Y. Yukselen-Aksoy, A. Kaya, A study of factors affecting on the zeta potential of kaolinite and quartz powder, Environ. Earth Sci. 62 (2011) 697–705, https://doi.org/10.1007/s12665-010-0556-9.
[79] K. Khawmee, A. Suddhiprakarn, I. Kheoruenromne, B. Singh, Surface charge properties of kaolinite from Thai soils, Geoderma 192 (2013) 120–131, https://doi.org/10.1016/j.geoderma.2012.07.010.
[80] Y. Liu, N. Jiang, M. Lyu, J. Wei, G. Wei, X. Han, Q. Shang, Q. Zhang, Y. Liu, H. Liu, X. Shi, TiO2/black phosphorus heterojunction modified by Ag nanoparticles for efficient photoelectrochemical water splitting, Mater. Chem. Phys. 301 (2023), https://doi.org/10.1016/j.matchemphys.2023.127624.
[81] K. Du, W. Yang, S. Deng, X. Li, P. Yang, High-quality black phosphorus quantum dots fabricated via microwave-tailored technology, Nanomaterials 10 (2020), https://doi.org/10.3390/nano10010139.
[82] X. Zhuang, Y. Wan, C. Feng, Y. Shen, D. Zhao, Highly efficient adsorption of bulky dye molecules in wastewater on ordered mesoporous carbons, Chem. Mater. 21 (2009) 706–716, https://doi.org/10.1021/cm8028577.
[83] A. Vinu, V. Murugesan, O. Tangermann, M. Hartmann, Adsorption of cytochrome c on mesoporous molecular sieves: influence of pH, pore diameter, and aluminum incorporation, Chem. Mater. 16 (2004) 3056–3065, https://doi.org/10.1021/cm049718u.
[84] Q. Liu, H. Peng, X. Tian, J. Guo, Synthesis of chrysotile based nanocomposites for tuning band gap and photocatalytic property, Appl. Clay Sci. 199 (2020), https://doi.org/10.1016/j.clay.2020.105885.
[85] H. Peng, D. Wu, H. Wan, L.L. Jia, G. Chen, J. Li, Y. Cao, X. Liu, R. Ma, Facile synthesis and characterization of halloysite@W18O49 nanocomposite with

enhanced photocatalytic properties, Appl. Clay Sci. 183 (2019), https://doi.org/10.1016/j.clay.2019.105319.
[86] I. Ahmad, R. Bousbih, A. Mahal, W.Q. Khan, M. Aljohani, M.A. Amin, N.N.A. Jafar, M.S. Jabir, H. Majdi, A.S. Alshomrany, M. Shaban, I. Ali, H. Bayahia, Recent progress in ZnO-based heterostructured photocatalysts: a review, Mater. Sci. Semicond. Process 180 (2024), https://doi.org/10.1016/j.mssp.2024.108578.
[87] I. Ahmad, S.A. AlFaify, K.M. Alanezi, M.Q. Alfaifi, M.M. Abduljawad, Y. Liu, Improved hydrogen production performance of an S-scheme Nb2O5/La2O3 photocatalyst, Dalton Trans. 54 (2024) 1402–1417, https://doi.org/10.1039/d4dt02913e.
[88] I. Ahmad, S. Shukrullah, M.Y. Naz, M.A. Rasheed, M. Ahmad, E. Ahmed, M. S. Akhtar, N.R. Khalid, A. Hussain, S. Khalid, Boosted hydrogen evolution activity from Sr doped ZnO/CNTs nanocomposite as visible light driven photocatalyst, Int J. Hydrog. Energy 46 (2021) 26711–26724, https://doi.org/10.1016/j.ijhydene.2021.05.164.
[89] I. Ahmad, S. Shukrullah, M.Y. Naz, H.N. Bhatti, A Cu medium designed Z-scheme ZnO-Cu-CdS heterojunction photocatalyst for stable and excellent H2 evolution, methylene blue degradation, and CO2 reduction, Dalton Trans. 52 (2023) 6343–6359, https://doi.org/10.1039/d3dt00684k.